

Universiteit
Leiden
The Netherlands

Silicon pore optics for high-energy optical systems

Girou, D.A.

Citation
Girou, D. A. (2022, June 14). *Silicon pore optics for high-energy optical systems*. *Casimir PhD Series*. Retrieved from https://hdl.handle.net/1887/3420652

Version:	Publisher's Version
License:	Licence agreement concerning inclusion of doctoral thesis in the Institutional Repository of the University of Leiden
Downloaded from:	https://hdl.handle.net/1887/3420652

Note: To cite this publication please use the final published version (if applicable).

SILICON PORE OPTICS FOR HIGH-ENERGY OPTICAL SYSTEMS

Proefschrift

ter verkrijging van
de graad van doctor aan de Universiteit Leiden,
op gezag van rector magnificus prof.dr.ir. H. Bijl,
volgens besluit van het college voor promoties
te verdedigen op dinsdag 14 juni 2022
klokke 16.15 uur

door

David Alain Girou

geboren te Saint-Michel d'Entraygues (France)
in 1989

Promotor:	Prof. dr. M.W. Beijersbergen
Copromotor:	Prof. dr. M.A.G.J. Orrit
Promotiecommissie:	Dr. M. Bavdaz (ESA-ESTEC, Noordwijk, The Netherlands)
	Dr. D.D.M. Ferreira (DTU, Kgs. Lyngby, Denmark)
	Prof. dr. J. Aarts
	Prof. dr. E.R. Eliel
	Prof. dr. ir. T.H. Oosterkamp





Casimir PhD series, Delft-Leiden 2022-14

ISBN 978-90-8593-525-4

An electronic version of this thesis can be found at:
`https://openaccess.leidenuniv.nl`

The present work is financially supported by cosine Research B.V.:
`https://cosine.nl/`

The front and back cover show stacks of thirty-five silicon plates directly bonded on top of each other, forming a pore-like structure. High-energy photons enter these pores at low grazing angles, where they are reflected on the reflective side of each plate, and exit the stack at the opposite end. Images are courtesy of cosine Research B.V.

CONTENTS

1 Introduction **1**
1.1 Silicon Pore Optics (SPO) concept . . . 2
1.2 The astrophysics case . . . 3
1.3 Thesis outline . . . 6
References . . . 8

2 Silicon Pore Optics realization **11**
2.1 Introduction . . . 12
2.2 Production of SPO mirror plates . . . 12
2.3 Development of coatings . . . 13
2.4 Cleaning and activation . . . 16
2.5 Stacking of mirror plates . . . 16
2.6 Stacking robots . . . 17
2.7 Mirror modules . . . 19
2.8 Ruggedisation . . . 20
2.9 X-ray characterization . . . 24
2.9.1 SPO stack characterization . . . 24
2.9.2 X-ray optical unit and mirror module characterization . . . 27
2.10 Conclusions and outlook . . . 28
References . . . 29

3 Plasma etching of silicon pore optics before coating deposition **33**
3.1 Introduction . . . 34
3.2 Evaluating the impact of plasma etching on surface roughness . . . 34
3.3 Investigating coating stability on non-patterned SPO plates . . . 36
3.4 Validating coating stability on patterned SPO plates . . . 37
3.5 Conclusions and discussion . . . 40
References . . . 43

4 Laue lens for radiation therapy with hard X-ray photons **45**
4.1 Introduction . . . 46
4.2 Silicon Laue components . . . 47
4.3 Lens design method . . . 50
4.3.1 System parameters . . . 50
4.3.2 System constraints . . . 51
4.3.3 Dimensions and shape of the focus . . . 52
4.3.4 Energy versus convergence angle . . . 53
4.3.5 Diffraction orders . . . 53
4.3.6 SiLC reflectivity and spectrum . . . 54
4.3.7 SiLC Simulation Code (SSC) . . . 54

4.4 Optimized lens design 55
4.4.1 Decisions on the system parameters 55
4.4.2 Optimization process 56
4.4.3 Performance 57
4.5 Conclusions and future work 60
References 62

5 Conclusions and outlook **67**
References 71

Summary **73**

Samenvatting **75**

List of Publications **77**

Curriculum Vitæ **79**

Acknowledgements **81**

1

INTRODUCTION

Parts of this chapter are based on an invited chapter for the Handbook of X-ray and Gamma-ray Astrophysics (Eds. C. Bambi and A. Santangelo, Springer Singapore, expected in 2022). Contributors to this invited chapter are Nicolas M. Barrière[1], Marcos Bavdaz[2], Maximilien J. Collon[1], Ivo Ferreira[2], David Girou[1], Boris Landgraf[1], and Giuseppe Vacanti[1].

[1] cosine measurement systems, Warmonderweg 14, 2171 AH Sassenheim, The Netherlands.
[2] European Space Agency, ESTEC, Keplerlaan 1, 2200 AG Noordwijk, The Netherlands.

1

1.1 Silicon Pore Optics (SPO) concept

The high-energy (short wavelength) region of the electromagnetic spectrum corresponding to the X-ray and soft Gamma-ray ranges presents a particular challenge to the development of efficient reflective optical elements such as mirrors for focusing optics. The reason being that at normal incidence, the reflectance of any "regular" mirror is close to nothing. On the other hand, for low grazing incidence angles, total external reflection or multilayer coatings using principle of optical interference can reach reflectances that are several times larger than those possible using normal incidence mirrors. Furthermore, other principles for focusing high-energy photons include Bragg diffraction in the volume of symmetrically cut crystals (referred to as Laue geometry). As a result, these techniques enable opportunities for high-energy optical systems applications in a variety of scientific and technological disciplines ranging from space-based astronomy (see Section 1.2), to medical [1], and material analysis.

Silicon pore optics (SPO) technology uses commercially available monocrystalline double-sided super-polished silicon wafers as a basis to produce high-energy photons mirrors. In addition to its direct bonding property [2, 3], silicon is rigid, has a relatively low density, very good thermal conductivity, excellent surface finish, both in terms of figure and surface roughness, making it a superb base material to build X-ray mirrors. SPO development leverages the massive investments done in the semiconductor and automotive industry, which made high-performance equipment, tools, materials, and processes available on the market allowing high-quality mass production. Standard wafers are produced with outstanding quality for a modest cost: prime grade double-sided super-polished monocrystalline 300 mm silicon wafers have specifications of 0.1 nm root mean square (RMS) surface roughness and total thickness variation (TTV) of less than 0.2 μm [4] (see Figure 1.1).

SPO substrates, also called mirror plates or simply plates, are cut out of wafers and carved out on one side in a regular pattern to leave thin parallel walls called ribs. In other words, plates consist of a thin membrane with a smooth reflective surface on one side and ribs along the plate length on the other. Consequently, stacking plates results in a pore-like structure, hence the name silicon pore optics.

The plates are attached to each other thanks to direct silicon bonding, which requires no adhesives. To produce a focusing optic, the mirrors must be curved. Starting from a mandrel that imposes the shape, plates can be stacked while preserving the mandrel figure in each plate. This results in a self-standing stack of elastically deformed mirror plates reproducing the shape of a mandrel that forms lightweight, high-resolution, X-ray optics (see Figure 1.2). In such a stack, X-ray photons enter pores at low-grazing angles, where they are reflected on the reflective side of each plate, and exit the optics at the opposite end.

Typical X-ray focusing optics uses nested shells to fill the available aperture and maximize effective area because low grazing incidence angles are needed for X-ray reflec-

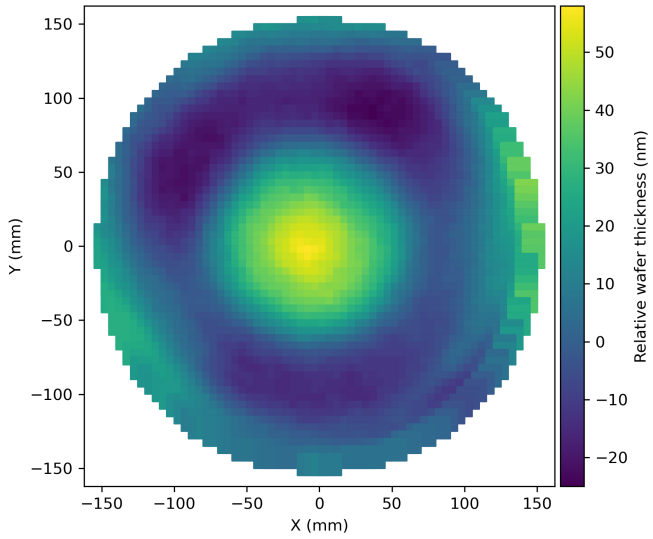


Figure 1.1: Typical relative thickness map of a silicon wafer for SPO plate production. The data is plotted relative to the median thickness of 775110 nm of the wafer. The thickness is measured by Fizeau interferometry.

tions. Because the ribs act as spacers between mirror plates, SPO can achieve an extreme packing density of the shells. The stiffness obtained by the bonded plates makes it possible to reduce the thickness of the membranes without impacting the figure accuracy, in a lightweight structure leading to large open area ratio.

SPO can be made to comply to many optical geometries, with the Wolter I [5] configuration being in general the most attractive for high-energy astrophysics applications. Two reflections are required to form an imaging system at grazing angles of incidence; this is achieved by placing two stacks, a primary stack and a secondary stack, in series along the path of the incoming photons. Two brackets, to which the stacks are glued, are used to fix the relative orientation of stacks, and provide a mechanical interface for integration in a larger structure.

1.2 The astrophysics case

The launch of the high-energy astrophysics observatories XMM-Newton [6] and Chandra [7], in 1999, marked the culmination of two major optics development efforts, and made observations of the X-ray sky with unprecedented sensitivity. Significant investments were required, and two different optics technologies developed to make these missions possible. The optics of XMM-Newton is based on electro-formed nickel, replicated from precision mandrels; it maximises effective area to make high-resolution spectroscopy of distant sources possible [8]. The Chandra optics, on the other hand, optimises the angular resolution at the cost of mass and effective area to provide high-

1

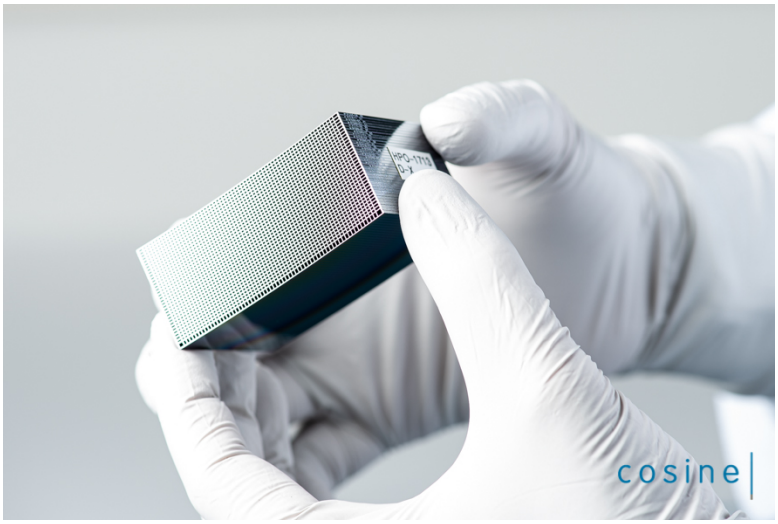


Figure 1.2: A stack of 34 SPO plates, with an outer radius of 737 mm.

resolution imaging. After more than two decades of active operations, these two missions remain in high demand for their stand-alone capabilities and the synergies with observations at other wavelengths. Their systems are, however, ageing, and the need for higher performance continues to increase.

The next generation of high-energy astrophysics observatories will have to reach deeper into the Universe, keeping pace with the present and future ground and space-based observatories like the James Webb Space Telescope, the Square Kilometer Array (SKA), and the Extremely Large Telescope (ELT). More photons will have to be collected from very distant sources, requiring larger effective area, a good angular resolution to avoid source confusion, and more sophisticated detector instruments.

In 2014, the European Space Agency (ESA) selected the Advanced Telescope for High-ENergy Astrophysics (Athena) as the second large-class mission designed to address the "Cosmic Vision" science theme "The Hot and Energetic Universe" [9]. This X-ray space telescope will rely on a novel type of optics, which was specifically invented and developed for the Athena mission: the Silicon Pore Optics (SPO) [10, 11].

The challenge of the Athena optics is the need to simultaneously comply with three technical requirements:

- Provide a large effective area (1.4 m^2 at 1 keV),
- Provide a good angular resolution (5 arcsec HEW),
- Remain in the mass allocation (around 1000 kg).

XMM-Newton and Chandra required different optics technologies, because they had to deliver different combinations of these three parameters. This is also true for the other X-ray missions flown to date, from Exosat [12], Einstein [13], ASCA [14] and Rosat [15], to BeppoSAX [16], Hitomi (Astro-H) [17], NuSTAR [18], and eRosita [19]. The optics for each of these missions is an engineering masterpiece, and each required substantial effort, skill, time, and funding to be developed, as well as for the flight models to be produced.

In Figure 1.3 the optics for each of these missions is compared, considering the aforementioned three parameters. The area density of the respective optics, expressed as effective area per mass of the optics is plotted against the resolving power of the optics, expressed as angular resolution elements per arcminute [20]. A clear correlation is observed despite the fact that the optics technologies are very different, ranging from foil-based optics to replicated optics and monolithic optics. Each of these systems was developed and built with large effort, and each represents a major achievement, but they all follow a power law correlation. Even the Chandra optics, the result of extraordinary investment in engineering and funding, manages to move only very slightly to the upper right side of the correlation line. The same is true for eRosita, which represents the highly optimised third generation of electroformed nickel technology.

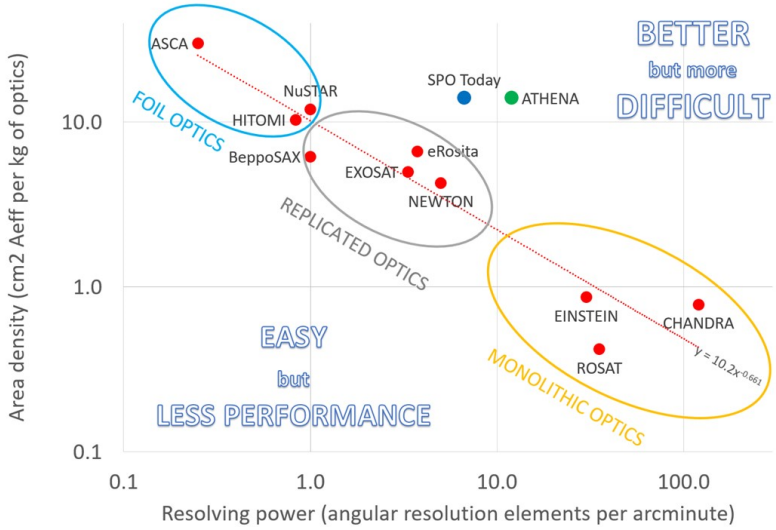


Figure 1.3: Characteristics of the optics flown on X-ray missions to date (red dots), plotting the area density of the optics (i.e. cm^2 of effective area per kg of optics) as function of the resolving power of the optics (i.e. number of angular resolution elements resolved by the optics in one arcminute). The characteristics of the X-ray optics flown to date show a clear correlation, described by a power law. Athena requires optics which cannot be achieved with the X-ray optics technologies flown to date. Adapted from [20].

The graph illustrates that it is possible to build lightweight optics with a large effective area, but lower angular resolution, or high resolution but heavy optics with a limited effective area. The power law allows only two of the three parameters (effective area,

angular resolution, and mass) to be optimised, but not all of them simultaneously. The optics required for the Athena mission (green dot in Figure 1.3) requires, however, a technological change to move away from this empirical power law into the "difficult corner" in the upper right of the graph. Linear extrapolation of all the X-ray missions flown to date using the three previous conventional technologies suggests that it would be possible to deliver the resolution and effective area, but it would require a mass of about 7000 kg, which is the mass of the complete Athena mission. Or it could respect the mass allocation of 1000 kg and deliver the effective area, but with a severely degraded angular resolution of about 1.6 arcminutes.

The SPO technology has already demonstrated the compliance with the Athena effective area and mass requirements. The angular resolution is approaching the Athena requirement as well, being already one order of magnitude better than what the established technologies could deliver for the same mass and effective area. The ongoing technological developments are focused on pushing the angular resolution to the required value. The technology pull generated by Athena resulted in the creation of a new type of X-ray optics, the SPO technology, which will undoubtedly also find other applications in demanding future space missions (the ARCUS mission studied by NASA is an example [21]).

1.3 Thesis outline

This thesis examines silicon pore optics by studying its design, modeling, manufacturing, testing, and characterization. Silicon pore optics is both an enabling technology for large space-borne X-ray telescopes such as Athena, and a versatile technology that can be further developed for gamma-ray optics, medical applications, and material research. The contents of this thesis are organized as follows:

In **Chapter 2** we explore how silicon pore optics are manufactured. We start by presenting how silicon pore optics plates are produced, coated, activated, and stacked into high-performance, self standing X-ray optics. Then, we further investigate how these stacks are assembled into mirror modules and characterized.

In **Chapter 3** we study in details how plasma eching enables the compatibility of thin film metallic coatings and direct bonding of silicon pore optics. First we ensure that plasma etching does not impact the low surface roughness required to achieve high imaging performance. Then we demonstrate that plasma etching before thin film deposition prevents unintentional removal of the metallic coatings during the activation step, making coating deposition compatible with direct bonding of silicon pore optics plates.

Finally **Chapter 4** proposes the design and modeling of a novel optical system composed of a Laue lens coupled to an X-ray tube that produces a focused beam in an energy range near 100 keV (λ = 12.4 picometer). One application of this system is radiation therapy, where it could enable treatment units that are considerably simpler and lower in cost than present technologies relying on linear accelerators. The Laue lens is made

of Silicon Laue Components (SiLCs), which exploit SPO technology, underlying the versality and potential of this technology.

1

References

[1] D. Girou, E. Ford, C. Wade, *et al.*, *Design and modeling of a laue lens for radiation therapy with hard x-ray photons,* Physics in Medicine & Biology **66**, 245007 (2021).

[2] M. Shimbo, K. Furukawa, K. Fukuda, and K. Tanzawa, *Silicon-to-silicon direct bonding method,* Journal of Applied Physics **60**, 2987 (1986).

[3] W. P. Maszara, G. Goetz, A. Caviglia, and J. B. McKitterick, *Bonding of silicon wafers for silicon-on-insulator,* Journal of Applied Physics **64**, 4943 (1988).

[4] B. Landgraf, M. J. Collon, G. Vacanti, *et al.*, *Development and manufacturing of SPO X-ray mirrors,* in *Optics for EUV, X-Ray, and Gamma-Ray Astronomy IX*, Vol. 11119, edited by S. L. O'Dell and G. Pareschi, International Society for Optics and Photonics (SPIE, 2019) pp. 107 – 114.

[5] H. Wolter, *Spiegelsysteme streifenden Einfalls als abbildende Optiken für Röntgenstrahlen,* Annalen der Physik **445**, 94 (1952).

[6] F. Jansen, D. Lumb, B. Altieri, *et al.*, *XMM-Newton observatory. I. The spacecraft and operations,* Astronomy and Astrophysics **365**, L1 (2001).

[7] M. C. Weisskopf, B. Brinkman, C. Canizares, *et al.*, *An Overview of the Performance and Scientific Results from the Chandra X-Ray Observatory,* The Publications of the Astronomical Society of the Pacific **114**, 1 (2002), arXiv:astro-ph/0110308 [astro-ph] .

[8] P. Gondoin, K. van Katwijk, B. R. Aschenbach, *et al.*, *X-ray spectroscopy mission (XMM) telescope development,* in *Space Optics 1994: Earth Observation and Astronomy*, Society of Photo-Optical Instrumentation Engineers (SPIE) Conference Series, Vol. 2209, edited by M. G. Cerutti-Maori and P. Roussel (1994) pp. 438–450.

[9] K. Nandra, D. Barret, X. Barcons, *et al.*, *The Hot and Energetic Universe: A White Paper presenting the science theme motivating the Athena+ mission,* arXiv e-prints , arXiv:1306.2307 (2013), arXiv:1306.2307 [astro-ph.HE] .

[10] M. Bavdaz and M. W. Beijersbergen, *Optical reflector element, its method of fabrication, and an optical instrument implementing such elements,* (2005).

[11] M. Beijersbergen, S. Kraft, R. Gunther, *et al.*, *Silicon pore optics: novel lightweight high-resolution X-ray optics developed for XEUS,* in *UV and Gamma-Ray Space Telescope Systems*, Society of Photo-Optical Instrumentation Engineers (SPIE) Conference Series, Vol. 5488, edited by G. Hasinger and M. J. L. Turner (2004) pp. 868–874.

[12] P. A. J. de Korte, J. A. M. Bleeker, A. J. F. den Boggende, *et al.*, *The X-Ray Imaging Telescopes on EXOSAT,* Space Science Reviews **30**, 495 (1981).

[13] L. P. van Speybroeck, *Einstein Observatory /HEAO-B/ mirror design and performance,* in *Space optics: Imaging X-ray optics workshop*, Society of Photo-Optical

Instrumentation Engineers (SPIE) Conference Series, Vol. 184, edited by M. Weisskopf (1979) pp. 2–11.

[14] P. J. Serlemitsos, L. Jalota, Y. Soong, *et al.*, *The X-Ray Telescope on board ASCA,* Publications of the Astronomical Society of Japan **47**, 105 (1995).

[15] J. Truemper, *The ROSAT mission,* Advances in Space Research **2**, 241 (1982).

[16] G. Conti, E. Mattaini, E. Santambrogio, *et al.*, *X-ray characteristics of the Italian X-Ray Astronomy Satellite (SAX) flight mirror units,* in *Advances in Multilayer and Grazing Incidence X-Ray/EUV/FUV Optics*, Society of Photo-Optical Instrumentation Engineers (SPIE) Conference Series, Vol. 2279, edited by R. B. Hoover and A. B. Walker (1994) pp. 101–109.

[17] T. Okajima, Y. Soong, P. Serlemitsos, *et al.*, *First peek of ASTRO-H Soft X-ray Telescope (SXT) in-orbit performance,* in *Space Telescopes and Instrumentation 2016: Ultraviolet to Gamma Ray*, Society of Photo-Optical Instrumentation Engineers (SPIE) Conference Series, Vol. 9905, edited by J.-W. A. den Herder, T. Takahashi, and M. Bautz (2016) p. 99050Z.

[18] F. A. Harrison, W. W. Craig, F. E. Christensen, *et al.*, *The Nuclear Spectroscopic Telescope Array (NuSTAR) High-energy X-Ray Mission,* The Astrophysical Journal **770**, 103 (2013), arXiv:1301.7307 [astro-ph.IM] .

[19] A. Merloni, P. Predehl, W. Becker, *et al.*, *eROSITA Science Book: Mapping the Structure of the Energetic Universe,* arXiv e-prints , arXiv:1209.3114 (2012), arXiv:1209.3114 [astro-ph.HE] .

[20] M. Bavdaz, E. Wille, M. Ayre, *et al.*, *Athena x-ray optics development and accommodation,* in *Optics for EUV, X-Ray, and Gamma-Ray Astronomy X*, Vol. 11822, edited by S. L. O'Dell, J. A. Gaskin, and G. Pareschi, International Society for Optics and Photonics (SPIE, 2021) pp. 32 – 46.

[21] R. K. Smith, *The Arcus soft x-ray grating spectrometer explorer,* in *Space Telescopes and Instrumentation 2020: Ultraviolet to Gamma Ray*, Vol. 11444, edited by J.-W. A. den Herder, S. Nikzad, and K. Nakazawa, International Society for Optics and Photonics (SPIE, 2020) pp. 377 – 383.

2

SILICON PORE OPTICS REALIZATION

Silicon Pore Optics (SPO) uses commercially available monocrystalline double-sided superpolished silicon wafers as a basis to produce mirrors that form low-mass high-resolution X-ray optics. The technology has been invented by cosine measurement systems and the European Space Agency (ESA) and developed together with scientific and industrial partners to mass production levels. It leverages techniques and processes developed over decades by the semiconductor industry to handle, process, and clean silicon wafers and plates. SPO is an enabling technology for large space-borne X-ray telescopes such as Athena, operating in the 0.2 to 12 keV band, with angular resolution aiming for 5 arc seconds.

Parts of this chapter are based on an invited chapter for the Handbook of X-ray and Gamma-ray Astrophysics (Eds. C. Bambi and A. Santangelo, Springer Singapore, expected in 2022). Contributors to this invited chapter are Nicolas M. Barrière[1], Marcos Bavdaz[2], Maximilien J. Collon[1], Ivo Ferreira[2], David Girou[1], Boris Landgraf[1], and Giuseppe Vacanti[1].

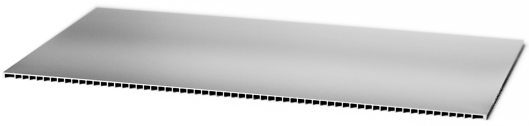
[1] cosine measurement systems, Warmonderweg 14, 2171 AH Sassenheim, The Netherlands.
[2] European Space Agency, ESTEC, Keplerlaan 1, 2200 AG Noordwijk, The Netherlands.

2.1 Introduction

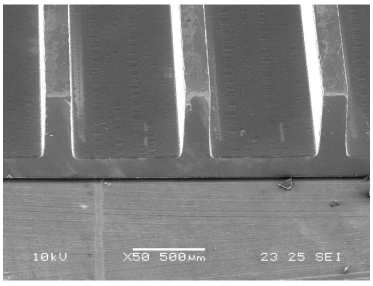
Silicon pore optics (SPO) are a new type of X-ray optics designed to enable future space-borne X-ray observatories such as Athena [1]. They are being developed by the European Space Agency (ESA), in collaboration with academic and industrial partners [2, 3]. These high-performance, modular, lightweight, yet stiff, high-resolution X-ray optics allow missions to reach an unprecedented large effective area of a few square meters, operating in the 0.2 to 12 keV band and with an angular resolution aiming at being better than 5 arc seconds. To this end, custom-made assembly tools and processes have been developed to build SPO using direct silicon bonding[4, 5]. SPO plates are single-sided ribbed rectangular silicon substrates assembled into high-performance optics by direct bonding them on top of each other. In this chapter, we present how silicon pore optics plates are produced, coated, activated, and stacked into high-performance, self standing X-ray optics. Then, we further investigate how these stacks are assembled into mirror modules and characterized.

2.2 Production of SPO mirror plates

With the technology spin-in from the semiconductor industry, mass production is being set up and standardized processes are being developed in order to manufacture SPO mirror plates in high quality, large quantity, and at relatively low cost. The production of SPO mirror plates starts with carving out ribs into 300 mm wafers. This process is effectively performed by removing material from the wafer down to the desired membrane thickness. Subsequently, rectangular plated are diced off the wafer, with the ribs along the direction of travel of the X-rays. The orientation of plate ribs and edges is aligned with the crystal planes of the silicon to ensure correct bending. The top side of the mirror plate is the reflective side (Figure 2.1, a)), and at the bottom is the ribbed side (Figure 2.1 b)) with the ribs parallel to each other. The plates currently manufactured have rib pitch varying from 1.0 mm to 2.4 mm with rib width of 0.17 mm.



(a)



(b)

Figure 2.1: (a) Example of a SPO mirror plate with its reflective side on top, and ribbed side facing down. (b) Scanning electron microscope image of the ribs of a SPO mirror plate.

The SPO mirror plates feature a thickness gradient along the rib direction to ensure that all the plates within a stack are confocal. The plane of the ribs is at an angle with the reflective side, referred to as the wedge angle. The challenge is to implement this angle with a linear profile, and without increasing the roughness of the surfaces. Two approaches have been developed to realize the wedge angle. A thickness gradient is either created by wet-chemical etching, or by IBF. A wedge accuracy better than 1% has been obtained with the wet-chemical processing, while the IBF is still under development. The advantage of IBF is that the TTV of wafers can be improved and reduced to potentially less than 10 nm in the same production step as the wedge processing.

Cleanliness is a crucial parameter for the production stacks. Particles on the plate surface can reduce bonding area and distort the optical figure. For this reason, SPO mirror plate production is performed in high-quality clean room environments of ISO 6 and ISO 5, and with specific equipment for also reducing the risk of organic contamination which can have a negative impact on the bondability of SPO mirror plates.

2.3 Development of coatings

The reflectivity of SPO mirror plates can be enhanced by deposition of thin-film coatings. The effectiveness of the coating is thereby described by the effective area of the optics. It depends on the collecting area and the efficiency of the mirrors in reflecting high-energy photons. The broadest energy window can be achieved with combinations of high-Z (e.g. Au, W, Mo, Pt and Ir) and low-Z materials (e.g. Si, SiC, C, DLC and B4C). Figure 2.2 shows an example of the computed on-axis effective areas for different reflective coatings for the Athena telescope energy range. The effective area is significantly larger with the addition of high-Z/low-Z bilayer coatings compared to the effective area of uncoated SPO mirror plates. In addition, multilayer coatings consisting of superimposed bilayers of high-Z/low-Z material can be applied to further increase the X-ray response of the optics at higher energies [6].

The SPO mirror plates feature a patterned coating on their reflective side in order to enable direct silicon bonding [4, 5] (see Section 2.5). The patterning of the coating is performed via optical lithography. This process, sketched in Figure 2.3, consists of the following steps. Firstly, a photosensitive polymer is deposited on the reflective side of the SPO mirror plate. In a second step, a patterned photoresist layer is created by exposing the photosensitive polymer to ultraviolet light and developing it by immersing the sample in a chemical solution. Subsequently, an X-ray reflective coating is deposited using a sputtering deposition technique. Finally, chemical lift-off is performed to remove the coated photoresist resulting in a patterned coated SPO mirror plate.

Direct current magnetron sputter deposition (MSD) has been applied for producing X-ray reflective coatings on mirrors of a number of X-ray telescopes, and as such, is a method with a good track record. It is a low-cost and well-controlled process. Particularly, iridium films with a thickness of 30 nm have been sputtered onto the Chandra telescope mirrors [8], and Pt/C and W/Si bilayer systems have been used for the NuSTAR

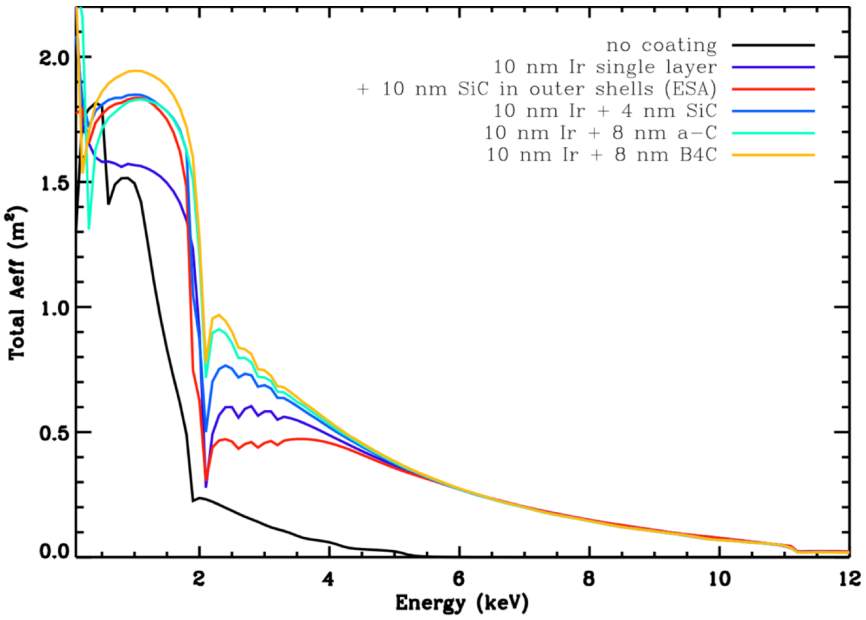


Figure 2.2: On-axis total effective areas for different reflective coatings for the Athena telescope energy range. Note that a significant increase in effective area can be expected at 1 keV if e.g. a B_4C overcoat is used. Credit: DTU [7].

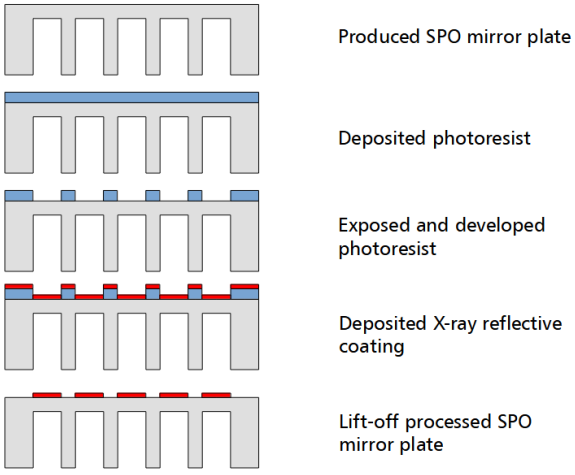
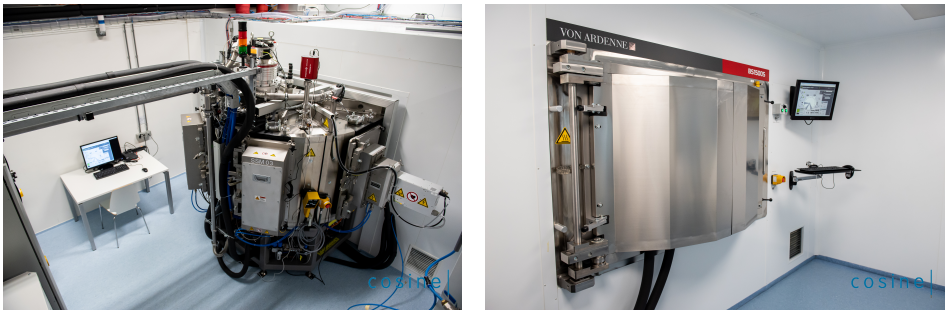


Figure 2.3: Schematic of optical lithography for SPO mirror plate with patterned X-ray reflective coating.

telescope mirrors successfully [9].

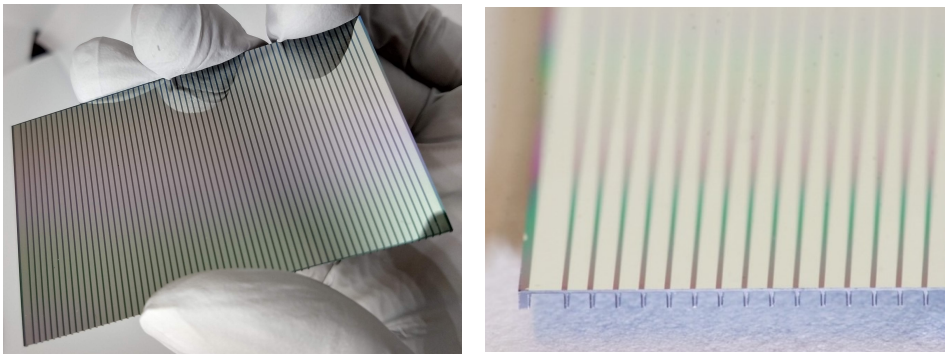
The SPO mirror plate coating process takes place at cosine using an industrial, high-throughput magnetron sputtering system [10] (Figure 2.4). It features three magnetrons for coating target materials and a plasma cleaning system in order to clean substrates from organic materials before a coating deposition run [11]. With this system, substrates as large as full 300 mm wafers can be coated with various high-Z materials such as tungsten, molybdenum, platinum and iridium and low-Z materials such as silicon, silicon carbide, carbon, diamond-like carbon, and boron carbide.



(a) (b)

Figure 2.4: Coating machine at cosine: (a) back side and (b) clean room side of the system.

The left photograph in Figure 2.5 shows an example of the reflective side of a produced patterned iridium-coated SPO mirror plate. In the right photograph, the coating stripes can clearly be distinguished from the silicon bonding areas.



(a) (b)

Figure 2.5: (a) SPO mirror plate with patterned coating of 10 nm iridium. (b) close-up view of a SPO plate with patterned iridium coating. The uncoated tracks are clearly visible above the ribs.



(a) (b)

Figure 2.6: Plate cleaning container (a) and fully automated wet bench (b) for chemical cleaning and activation of SPO mirror plates at cosine.

2.4 Cleaning and activation

Cleanliness is paramount to the SPO technology. The mirror plates are cleaned in industrial wet-benches with a SC-1 cleaning [12] and then dried.This results in hydrophilic ('activated') surfaces, free of particulate contamination or drying stains. The hydrophilic surfaces are key to direct silicon bonding, as explained in the next section.

The photographs in Figure 2.6 show the fully automated cleaning wet bench at cosine, which is used to prepare the SPO mirror plates for stacking.

2.5 Stacking of mirror plates

SPO stacks hold together and maintain their shape without adhesive between the mirror plates. This direct bonding process can take place at room temperature and is widely used to join glass or silicon surfaces to each other [4, 5]. The two mating surfaces need to be chemically prepared (i.e. activated) and need to be clean, smooth, and conforming for a direct bond to take place. After activation, a thin layer of OH- groups is present on both the ribbed and the reflective sides of each mirror, forming silanol (Si-OH) groups [13]. These absorbed water molecules form a bridge (Si-OH+HO-Si) across the two bonding surfaces that is maintained via Van-der-Waals forces for temperatures ranging from 10°C to 110°C [13]. Furthermore, post-stacking thermal treatment, such as annealing above 110°C, enables the silanol bonds to transform into stronger siloxane (Si-O-Si) bonds [13]. During annealing, the interface is drying steadily and siloxane bridges form across the bonding surfaces, but for temperatures below 1000°C, the bonding energy is limited by the area in contact, which is itself limited by surface roughness [13]. Annealing at temperatures above 1000°C can increase the contact area through viscous flow of the oxide, which then fills up the micro-gaps at the interface to form additional siloxane bonds [13]. However, environmental testing (see Section 2.8) indicates that the bond energy is large

enough to survive shock and vibration testing, meaning that annealing stacks at temperatures between 150°C and 1000°C is sufficient. Note that the excess water can also exude over time and siloxane linkage can form after months of storage [13].

The plates are stacked on a concave mandrel, starting with a plate placed with reflective side in contact with the mandrel and ribs pointing inwards, called base plate. The mandrel is polished with the design shape of the stack, can be cylindrical or conical, and can feature additional meridional curvature. The next plate is then brought into a similar shape as the base plate by using a die, a tool with the same figure as the mandrel. The plate is attached with the mirror surface to the die, resulting in the ribs pointing outwards. The two plates are brought into close contact such that the two sets of ribs make contact and that direct bonding starts. At this moment, the plate copies the shape of the mandrel and becomes the first reflective plate of the stack. The die then releases the plate and the process can be repeated, with the only difference that the next plates are bonded with their ribs to the mirror surface of the upper plate in the stack. At the end of the process, the stack is released from the mandrel and keeps the desired shape through the acting bond forces and the stiffening effect of the ribs. To achieve high angular resolution, it is important to replicate the initial figure of the mandrels with minimum systematic and stochastic errors. Cleanliness of the plates, mandrel and die is of prime importance to avoid degrading the figure with bumps created by trapped particles plate after plate. Systematic slope errors can be minimized with optimized plate design and stacking approach.

Note that when it is curved, the mandrel defines only the outer starting radius of a stack. With each plate added, the stacks' sagittal radius of curvature becomes smaller by the thickness of the mirror plate. In the case of double-reflection optical design, such as Wolter I, it is important to align the ribs to several microns. This minimizes the loss of open area as the two stacks are aligned behind each other.

2.6 Stacking robots

Automated stacking robots have been developed to meet the mass production and quality requirements of SPO technology: automation provides cost-efficiency, improves repeatability for large series, and ensures the highest standard of cleanliness. The robots are composed of a robotic arm equipped with a plate gripper, a die attached upside down, and a mandrel resting onto an hexapod (Figure 2.7). The hexapod is on a linear translation stage that allows moving the mandrel and the stack from the die to an optical metrology system.

The stacking process starts with a batch of several tens of plates loaded in a container that are cleaned and activated (Figure 2.6). The container is loaded into the robot, which is placed inside an ISO-class 5 clean area to keep the plates from particulate contamination. The robot extracts the first plate from the container, aligns it to the gripper, and places it on the mandrel, as described in Section 2.5. A second plate is extracted, aligned to the gripper and attached to the die with the ribs pointing downwards. The mandrel

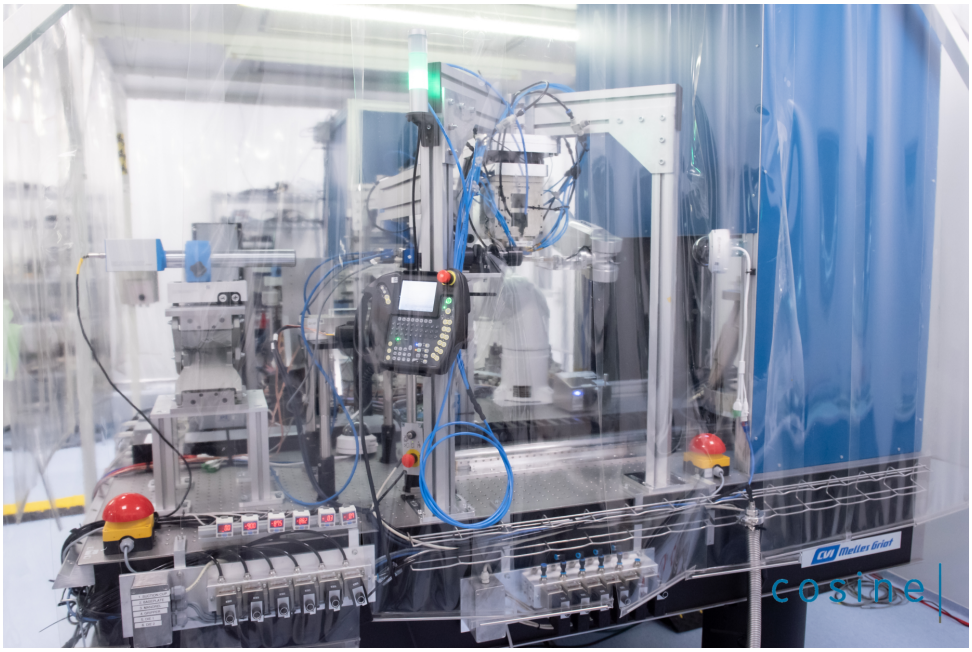


Figure 2.7: Stacking robot inside a cleanroom, as installed at cosine. It is equipped with a robotic arm to extract plates for stacking. A hexapod allows aligning the mandrel to the die. The blue box on the right is an optical metrology system that can measure the figure and cleanliness of each plate after having been stacked.

and die are brought into close contact until the ribs align and the bond is created. Then the die releases the plate. The first reflective plate is now bonded to the base-plate. The stack is translated to the in-situ metrology, which measures the figure of the bonded plate, determining not only the shape, but also the cleanliness and therefore the quality of the bond. The robot then proceeds to extract the next plate, attaching it to the die. The stacking process repeats, this time with the ribs bonding to the mirror surface of the stack on the mandrel.

The process repeats until the desired stack height is reached. Stacks between 10 and 70 plates have been manufactured, 35 plates being the most common so far. The stacking process takes about 5 minutes per plate and can run completely autonomously. Once the stack is finished, it is released from the mandrel and a final inspection is performed to measure the outer geometry and to visually check for defects.

Prior to stacking, the mandrel axis is aligned with the die axis. The plate gripper, which is the reference for the plates alignment, is also aligned with respect to the die and mandrel. A robot is configured for one specific set of stacks defined by its mandrels and plate types. The robot needs to be reconfigured to produce stacks of different radii, plate geometry or figure.

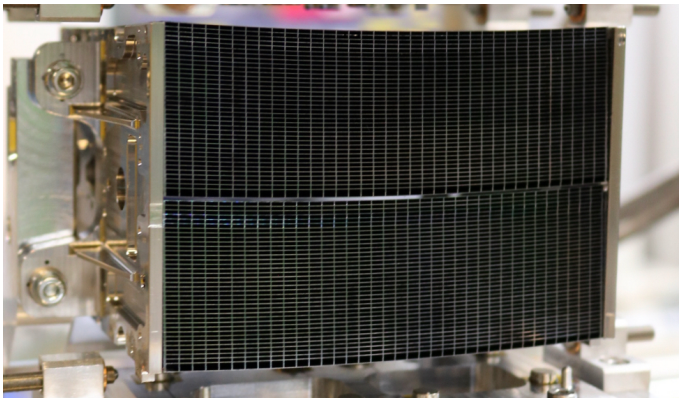


Figure 2.8: Row-08 MM seen from the exit side. The two secondary stacks are visible, each with 37 mirror plates in addition of their base plate. Bracket A, with its two ears, is visible in this view.

2.7 Mirror modules

SPO consists of stacks of mirror plates, which shape is driven by the mandrels used. In the case of a Wolter I optical design, two different stack shapes are needed: primary and secondary stacks for the two reflections. When aligned after each other, these stacks form a so-called X-ray optical unit (XOU). The fact that the primary and secondary stacks are initially disjoined represents a challenge as their relative alignment can influence greatly the optical quality of the XOU. It is required to co-align their optical axis and align the mirror plates ribs and membranes. Then this alignment must be frozen. This freezing is done by gluing two side plates, commonly referred to as brackets, to the stacks, forming a mirror module (MM). A MM is thus a self-standing X-ray focusing optics with mechanical interfaces. The development of MMs has been been driven by Athena so far. In the current design, Athena MMs are made of two XOUs co-aligned to be confocal, glued within one pair of brackets (Figure 2.8).

The brackets are made of an austenitic nickel-iron alloy containing 36% nickel (Invar 36), a material with very low coefficient of thermal expansion of 1.2×10^{-6} K^{-1}, close to that of silicon 2.6×10^{-6} K^{-1}. Their role is to freeze the alignment of the stacks, protect the stacks, provide interfaces between the MM, and any support structure or mount, and provide a mechanical reference for the optical axis of the MM. The brackets can also provide interfaces to baffles or aperture mask. Low-outgassing and low-shrinkage epoxy is used to fixate the brackets to the sides of the stacks. The interface points of the brackets are called *ears* (visible on the right hand side of Figure 2.8).

The alignment strategy is as follows [14, 15]: the brackets are aligned with respect to each other using a tool providing six degrees of freedom to each bracket. The primary stack is then glued within the brackets. This alignment relies on mechanical metrology with a coordinate measurement machine (CMM). This assembly is then brought

to a synchrotron facility where a monochromatic, low-divergence, X-ray pencil beam is available. Currently this is done at the X-ray Parallel Beam Facility 2 (XPBF 2) synchrotron beamline, which is installed in the laboratory of the Physikalisch-Technische Bundesanstalt (PTB) at the synchrotron radiation facility BESSY II in Berlin [16]. An additional beamline is planned to become operational in 2022 at the ALBA synchrotron facility in Barcelona [17]. XPBF 2, tailored for the development of Athena's MMs, provides a 1-keV beam monochromatized and collimated by a toroidal mirror with multi-layer coating, allowing beam dimensions between 0.05×0.05 mm^2 and 7×7 mm^2. The detector is placed at 12 m $\pm$ 0.5 m from the sample, and its position is monitored by a laser tracker.

At XPBF 2, the direction of the incident beam is used as optical axis for the MM. The primary stack, already glued within the brackets, is aligned to bring its optical axis parallel to the beam. Then the secondary stack is brought in and the rest of the alignment is done in double reflection. The secondary stack is aligned with respect to the first stack to minimize the intersection of the ribs and membrane (i.e. maximize throughput of the XOU), bring the PSF at the nominal position, and obtain the best possible optical quality (co-align the stacks' optical axes).

Pencil beam raster scans are used to determine the three-axis orientation of the primary stack with respect to the beam, as well as of the secondary stack with respect to the primary stack [14]. The position of incidence of the beam onto the primary stack as well as the position of the beamspot recorded on the camera are reconstructed in a common coordinates system. An analytical three-dimensional model of the optic is used in a ray-trace function that transforms incident position into position on the camera. This function is used to fit the orientation of a stack in single reflection or double reflection. This method allows precise and deterministic alignment.

2.8 Ruggedisation

As SPO development progresses, it is necessary to validate the technology under launch and orbit environmental conditions [18]. Payloads undergo high levels of vibrations and shocks during the rocket launch and fairing separations. It is therefore crucial to check that the MMs are robust enough to withstand such conditions and ensure that their mechanical stability and optical performance will remain stable before, during, and after launch. Environmental testing also allows identifying potential design issues and correcting them. This is the process of ruggedisation where a piece of equipment is made stronger and more resistant.

Thanks to its modular nature, SPO can be tested at MM level. MMs are submitted to vibration and shock tests, in accordance with Athena's launch vehicle and mission requirements. The MMs are characterized with X-ray before and after each test to verify that the optical performance remains unchanged (Section 2.9). MMs are first integrated into a device under test (DUT, see Figure 2.9) that is representative of a mirror structure and enables interfacing the MM with test equipment (shock table, shaker, vacuum

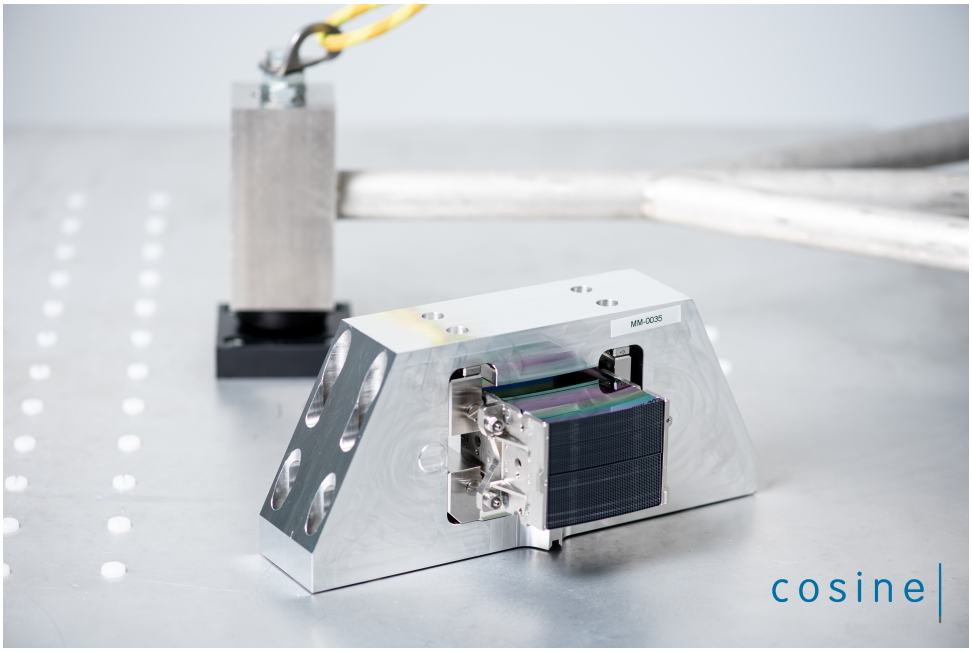


Figure 2.9: MM integrated into a device under test (DUT), laying on a shock table. The hammer can be seen resting on an anvil in the background.

chamber).

Vibration testing consists of two steps performed successively: sine qualification and random qualification tests. Two triaxial acceleration sensors (pilots) are mounted to the test mount to control the shaker input to the MM. The dynamic response of the MM is monitored on both brackets, close to the MM center of mass. Two single axis accelerometers are also used to monitor the dynamic transfer over the mechanical shims. These mechanical shims are used to preload the dowel pin (DP) flexures used to mount the MM, and to statically mimic the expected dynamic structural distortions of the mirror structure during low frequency (sine) and vibro-acoustic (random) mission phases. The Athena sine qualification test levels are shown in Table 2.1.

For the random test, Athena qualification and used notched levels are presented in Table 2.2. All random runs at qualification level are preceded by a low level ramp up, meaning a sequence of runs at -12 dB, -9 dB, -6 dB, and -3 dB for 30 seconds each. These runs are used to predict the 0 dB response levels at the MM center of mass and to check that the design limit load (DLL) values are not exceeded.

Frequency signature test runs (also called resonance searches) are performed before and after each high level qualification test run to detect any potential changes in structural behavior of the MM or test setup. A test run is considered successful if the change

Table 2.1: Athena sine qualification test levels for in-plane and out-of-plane directions.

Excitation direction	Frequency	Amplitude	Sweep rate
In-Plane (X, Y)	5 Hz 17 Hz 100 Hz	±11 mm 13 g 13 g	2 Oct/min
Out-of-plane (Z)	5 Hz 19 Hz 100 Hz	±11 mm 16 g 16 g	2 Oct/min

Table 2.2: Athena random qualification test levels with notching. Each test shall last 2 min per axis.

Direction	Frequency	Power Spectral Density (PSD)	Overall input
X	20-100 Hz 100 Hz 100-200 Hz 200-400 Hz 400-2000 Hz	+10 dB/Oct 0.05 g^2/Hz 0.20 g^2/Hz 0.05 g^2/Hz -15 dB/Oct	9.3 g-rms
Y	20-100 Hz 100 Hz 100-200 Hz 200-400 Hz 400-2000 Hz	+10 dB/Oct 0.05 g^2/Hz 0.20 g^2/Hz 0.05 g^2/Hz -15 dB/Oct	9.3 g-rms
Z	20-100 Hz 100 Hz 100-200 Hz 200-400 Hz 400-2000 Hz	+10 dB/Oct 0.05 g^2/Hz 0.70 g^2/Hz 0.05 g^2/Hz -15 dB/Oct	6.0 g-rms

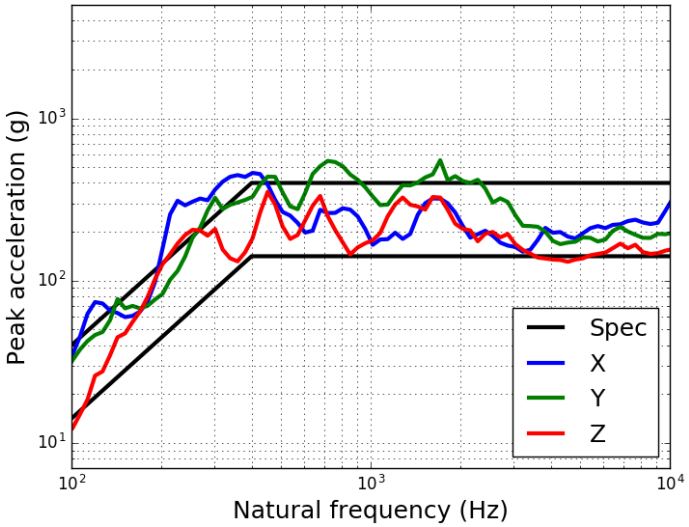


Figure 2.10: Shock Response Spectrum (SRS) of the shock applied to a MM. The qualification level with a margin of +6 dB and -3 dB define a specification (spec) band delimited by the black lines in the plot. Despite the peak acceleration being outside of the specification band for some frequencies, this SRS is considered excellent, and the test successful.

in frequency is less than 5%.

Shock testing is performed with a shock table and shock levels are defined by a shock response spectrum (SRS). Mechanical shims are used to preload the DP flexures similarly to the vibration test. There, the preloading and SRS level simulate mirror structure distortions during one of the most dramatic event of the launch sequence as seen by the payload: the fairing separation. Figure 2.10 displays a SRS as measured on the test mount (also called input SRS) of a MM. Note that the SRS is isotropic, enabling the testing of all three axis in a single shock. Two high-speed cameras, each looking at one side along the optical axis, are used to assist in identifying failures, as well as their modes. Resonance searches are also performed to check on the structural integrity of the MM.

SPO stacks have been tested as standalone items, then again once assembled into a MM for the different radii used for development (representative of the inner-most, middle, and outer-most radii of Athena). At the time of writing, the actual Athena flight configuration is also starting to be tested with the first row-08 MM having passed vibrations tests at qualification levels. Such testing campaigns at qualification levels will continue and extend to all rows of Athena, further ruggedizing SPO technology in general. For the flight model of Athena, each MM will undergo a workmanship test consisting of random vibration tests at acceptance level; additional environmental tests will be conducted at the mirror assembly level once the MM are integrated into the mirror structure.

2.9 X-ray characterization

Optical metrology of the SPO stacks taken during manufacturing produces a wealth of information on the eventual performance of the optics at X-rays. However, regular X-ray characterization remains an important part of the development process of the optics, as it is done at the same energy and incidence angle used during the actual use of the optics.

2.9.1 SPO stack characterization

Given the number of SPO stacks that are made, and the fact that individual stacks are not imaging systems, it has long been recognized that a dedicated facility with a high flux of X-rays is required to meaningfully support the development of the optics [19–22]. Characterization by means of a low-divergence (≈ 1 arcsec) pencil beam of X-rays, as opposed to the more customary full-flood illumination, makes it possible to probe the surface of each plate in a stack with high spatial resolution, and arrive at the characterization of the surface slope errors and of the millimeter-scale defects contributing to the widening of the beam. At the time of writing, two dedicated beamlines are available in the PTB laboratory at the BESSY II synchrotron [20, 22], and an additional beamline is being assembled at ALBA [17] (Section 2.7).

Samples are characterized by moving them in a rectangular pattern of columns and rows through a $100 \times 100\,\mu\text{m}^2$ X-ray beam. In Figure 2.11 we show how the samples are placed in the beam and measured. Scan columns are spaced usually by ≈ 2 mm, and scan rows are spaced by $100\,\mu$m. This so-called *standard scan pattern* probes only a fraction (about 5 %) of the total reflecting area in an SPO stack. Tests have shown that the results obtained in this manner are representative of the complete surface. That is, making the scan columns more densely spaced, or using overlapping beams, does not add new information on the properties of the stack derived from the data.

The data collected during a standard scan is processed to identify and isolate the reflected X-ray beam, then characterized by its centroid and RMS length and width. After this morphological characterization, the positions of the images and the sample in the laboratory frame are determined and converted to a common coordinate frame for further analysis. Each reflected beam probes between 5 and 10 mm along each of the pores, depending on the type of stack and the angle of incidence used in the measurement. Maps of the variation of the RMS length of the images already reveal good and bad areas on each plate.

A global quality indicator of the properties of the reflecting surface is derived by superimposing all the reflected images on their barycenters and calculating the half energy width (HEW) of the resulting image. This indicator is called the *on centroid performance* of the sample and is usually expressed in units of the HEW of the direct beam, and it represents the average surface quality on length scales of the order of a few to several millimeters.

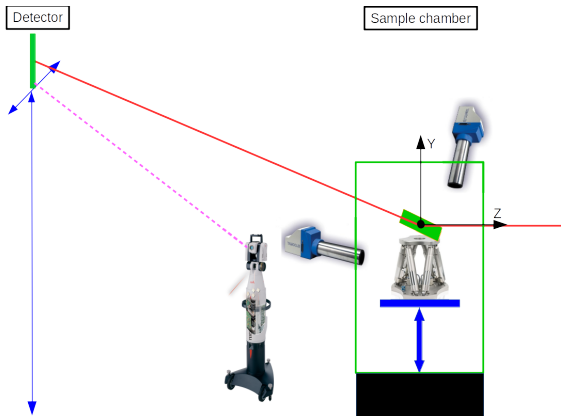


Figure 2.11: Logical view of a beamline dedicated to the assembly and characterization of SPO. The synchrotron X-ray beam travels from positive to negative Z (red). The sample is loaded inside a vaccum chamber (green) on a platform with six degrees of freedom and moved in front of the X-ray beam. During a measurement, the incidence angle of the X-ray is kept constant through the use of two autocollimators. The reflected beam is intercepted by a detector, whose position is monitored with a laser tracker.

More complex metrics can be obtained by processing the data further. A model of the stack is introduced, and the expected position of the barycenters of the reflected X-ray beam is calculated. By comparing the expected and the measured positions, a displacement vector is obtained for each reflected image. All the images are then superimposed on the common barycenter, where they would all end up if the SPO stack behaved ideally, and shifted by the displacement vector calculated. The HEW of the resulting image (Figure 2.13) is a metric of the optical quality of the stack, and it represents the contribution of the stack to the optical quality of a pair of stacks arranged to form an imaging system. This indicator is called the *on-model centroid performance* of the sample.

Data from the raster measurement can be used to derive a variety of performance indicators related to the optical quality of the stack. We mention here three of them, illustrated in Figure 2.12, they are:

- The broadening of the reflected beam, a marker of short length-scale errors;
- The (best-fit) meridional curvature, a marker of global figure errors;
- The difference between the measured and expected position of the reflected beam taking into account the best-fit meridional curvature, a marker of long length-scale figure errors.

The same analysis that leads to the calculation of the displacement vectors is also able to estimate the local surface normal seen by the X-ray beam, and the difference between ideal and actual surface normal. This information is coded in a *synoptic slope error map*, an example of which is shown in Figure 2.14. The map codes information

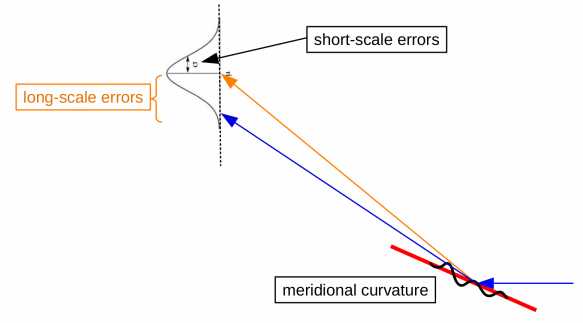


Figure 2.12: Depiction of the measurement process and three performance indicators derived from it. The X-ray beam enters from the right and impinges on a plate (in red) whose surface has some defects (represented by the black wavy line). These defects lead to a broadening of the reflected beam (short length-scale errors). The meridional curvature of the plate is also derived (global figure errors). Long-scale figure errors are arrived at by comparing the expected (blue arrow) and the measured (orange arrow) barycenter of the reflected beam, taking into account the best-fit meridional curvature.

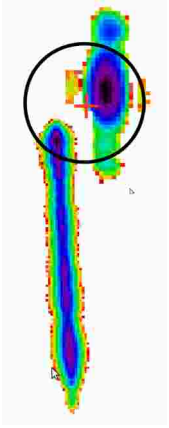


Figure 2.13: Illustration of the algorithm that leads to the construction of the on model centroid image for a stack. Shown are two of the reflected beam images. The cross at the center indicates the place where the barycenters of the reflected beams are expected to fall if the sample behaved ideally. A synthetic image, called the on model centroid image, is obtained by adding each reflected beam to it after applying the translation calculated during the analysis.

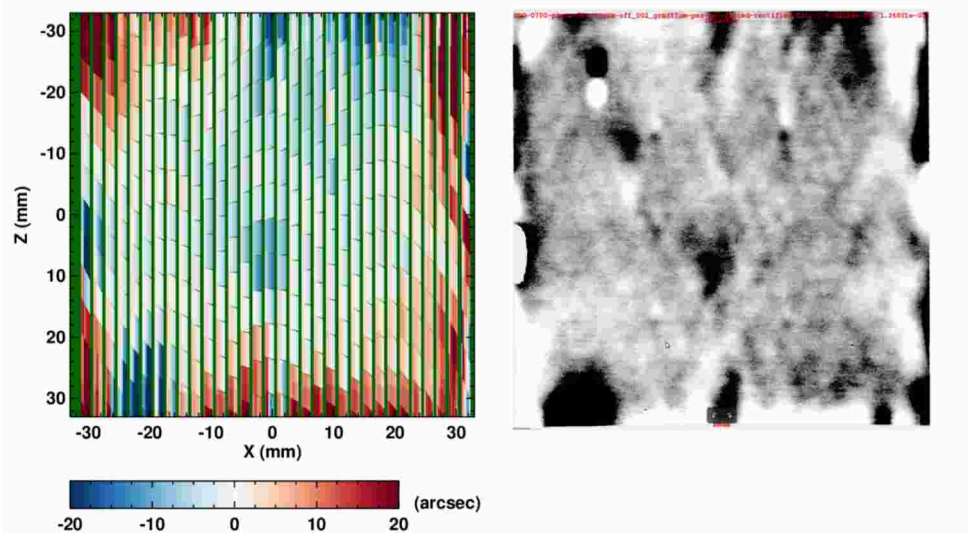


Figure 2.14: An example of a synoptic slope error map derived from X-ray data (left), compared to the cleanroom surface metrology for one of the plates in the same stack. The two independent datasets are in excellent agreement. Reproduced from [23].

for the entire stack: each block is made of a number of smaller rectangles, one for each plate, color coding the local slope error experienced by the X-ray beam (left to right for increasing plate number). These maps can be compared to similar per-plate maps obtained during manufacturing of the stack. It can be seen in the figure that the same features are visible in both maps. This proves that cleanroom metrology provides information that is immediately relevant for the X-ray behavior of the optics. The map also shows that the error experienced by the X-ray beam at each location is nearly the same irrespective of plate number. This shows that the shape of the first plate in the stack is almost exactly reproduced across the entire stack.

2.9.2 X-ray optical unit and mirror module characterization

Once assembled into an imaging system (XOU), a primary-secondary stack doublet can be characterized with the same standard scan used for the characterization of single stacks. The analysis of the data proceeds along the same lines described in the previous section, but now the individual images can be combined to arrive at an estimate of the HEW of the imaging system (Figure 2.15). Owing to the use of a pencil beam, it is now possible to analyze the performance of the optics along different axes, for instance by looking at how the HEW changes with plate number. Other spatial selections are possible, leading to the ability to compare the performance of different regions of the optics, that can be related to the indicators derived from the cleanroom metrology.

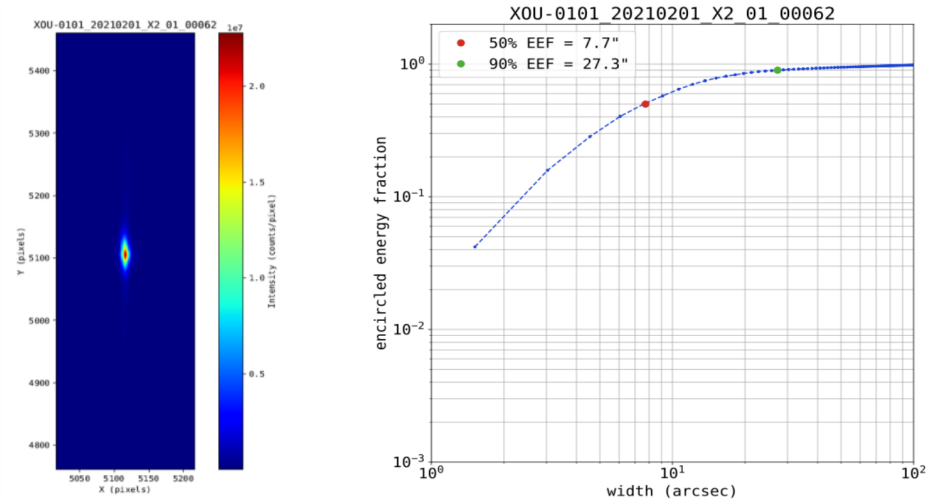


Figure 2.15: A sample PSF obtained by the algorithmic superposition of several thousands individual pencil-beam images. This particular image refers to the primary-secondary pair called XOU-0101, and it shows the result obtained for the central 70 % of the width of the sample. This has been a common data selection used during the development of SPO.

2.10 Conclusions and outlook

SPO uses technology spin-in developed for decades by the semiconductor and automotive industry, which have massively invested in the fabrication and processing of silicon wafers. It has become a very mature x-ray optics technology, thanks to the continuous development efforts to prepare the industrial production of Athena, the largest x-ray optics yet to be launched into space. SPO is an enabling technology for Athena, which could not aim for the combination of such a large effective area and high angular resolution with any other existing technology. The optics for Athena is under intense development, aiming to start manufacturing the first flight models MMs in 2026. SPO has also shown to be a versatile technology that can be further developed for gamma-ray optics and medical applications[24].

References

[1] M. Beijersbergen, S. Kraft, R. Günther, *et al.*, *Silicon pore optics: novel lightweight high-resolution X-ray optics developed for XEUS,* in *UV and Gamma-Ray Space Telescope Systems*, Vol. 5488, edited by G. Hasinger and M. J. L. Turner, International Society for Optics and Photonics (SPIE, 2004) pp. 868 – 874.

[2] M. Bavdaz, E. Wille, M. Ayre, *et al.*, *Optics developments for ATHENA,* in *Optics for EUV, X-Ray, and Gamma-Ray Astronomy IX*, Vol. 11119, edited by S. L. O'Dell and G. Pareschi, International Society for Optics and Photonics (SPIE, 2019) pp. 71 – 82.

[3] M. J. Collon, G. Vacanti, N. M. Barrière, *et al.*, *Status of the silicon pore optics technology,* in *Optics for EUV, X-Ray, and Gamma-Ray Astronomy IX*, Vol. 11119, edited by S. L. O'Dell and G. Pareschi, International Society for Optics and Photonics (SPIE, 2019) pp. 150 – 157.

[4] M. Shimbo, K. Furukawa, K. Fukuda, and K. Tanzawa, *Silicon-to-silicon direct bonding method,* Journal of Applied Physics **60**, 2987 (1986).

[5] W. P. Maszara, G. Goetz, A. Caviglia, and J. B. McKitterick, *Bonding of silicon wafers for silicon-on-insulator,* Journal of Applied Physics **64**, 4943 (1988).

[6] A. Jafari, D. D. M. Ferreira, S. Kadkhodazadeh, *et al.*, *Long-term performance and durability of Ir/B4C multilayer x-ray mirrors: focusing on composition, structure, and reflectivity properties,* Journal of Astronomical Telescopes, Instruments, and Systems **6**, 1 (2020).

[7] D. D. M. Ferreira, S. Svendsen, S. Massahi, *et al.*, *Performance and stability of mirror coatings for the ATHENA mission,* in *Space Telescopes and Instrumentation 2018: Ultraviolet to Gamma Ray*, Vol. 10699, edited by J.-W. A. den Herder, S. Nikzad, and K. Nakazawa, International Society for Optics and Photonics (SPIE, 2018) pp. 916 – 926.

[8] P. Gorenstein, *Focusing x-ray optics for astronomy,* X-Ray Optics and Instrumentation **2010** (2010), 10.1155/2010/109740.

[9] F. E. Christensen, A. C. Jakobsen, N. F. Brejnholt, *et al.*, *Coatings for the NuSTAR mission,* in *Optics for EUV, X-Ray, and Gamma-Ray Astronomy V*, Vol. 8147, edited by S. L. O'Dell and G. Pareschi, International Society for Optics and Photonics (SPIE, 2011) pp. 298 – 316.

[10] S. Massahi, F. E. Christensen, D. D. M. Ferreira, *et al.*, *Installation and commissioning of the silicon pore optics coating facility for the ATHENA mission,* in *Optics for EUV, X-Ray, and Gamma-Ray Astronomy IX*, Vol. 11119, edited by S. L. O'Dell and G. Pareschi, International Society for Optics and Photonics (SPIE, 2019) pp. 115 – 130.

[11] D. Girou, S. Massahi, D. D. M. Ferreira, *et al.*, *Plasma etching for the compatibility of thin film metallic coatings and direct bonding of silicon pore optics,* Journal of Applied Physics **128**, 095302 (2020), https://doi.org/10.1063/5.0010212 .

[12] W. KERN, *Cleaning solutions based on hydrogen peroxide for use in silicon semiconductor technology,* RCA Review **31**, 187 (1970).

[13] U. Gösele and Q.-Y. Tong, *Semiconductor wafer bonding,* Annual Review of Materials Science **28**, 215 (1998), https://doi.org/10.1146/annurev.matsci.28.1.215 .

[14] N. M. Barrière, G. Vacanti, S. Verhoeckx, *et al.*, *Assembly of confocal silicon pore optic mirror modules for Athena,* in *Optics for EUV, X-Ray, and Gamma-Ray Astronomy IX*, Society of Photo-Optical Instrumentation Engineers (SPIE) Conference Series, Vol. 11119 (2019) p. 111190J.

[15] N. M. Barrière, L. Babić, A. Bayerle, *et al.*, *Assembly of confocal silicon pore optics mirror modules,* in *Society of Photo-Optical Instrumentation Engineers (SPIE) Conference Series*, Society of Photo-Optical Instrumentation Engineers (SPIE) Conference Series, Vol. 11822 (2021) p. 1182208.

[16] E. Handick, L. Cibik, M. Krumrey, *et al.*, *Upgrade of the x-ray parallel beam facility XPBF 2.0 for characterization of silicon pore optics,* in *Society of Photo-Optical Instrumentation Engineers (SPIE) Conference Series*, Society of Photo-Optical Instrumentation Engineers (SPIE) Conference Series, Vol. 11444 (2020) p. 114444G.

[17] D. Heinis, A. Carballedo, C. Colldelram, *et al.*, *X-ray facility for the characterization of the Athena mirror modules at the ALBA synchrotron,* in *Society of Photo-Optical Instrumentation Engineers (SPIE) Conference Series*, Society of Photo-Optical Instrumentation Engineers (SPIE) Conference Series, Vol. 11852 (2021) p. 1185222.

[18] D. A. Girou, C. van Baren, I. te Kloeze, *et al.*, *Environmental testing of the Athena telescope mirror modules,* in *Optics for EUV, X-Ray, and Gamma-Ray Astronomy X*, Vol. 11822, edited by S. L. O'Dell, J. A. Gaskin, and G. Pareschi, International Society for Optics and Photonics (SPIE, 2021) pp. 47 – 55.

[19] M. J. Collon, S. Kraft, R. Günther, *et al.*, *Performance characterization of silicon pore optics,* (Orlando, Florida , USA, 2006) p. 62661T.

[20] M. Krumrey, L. Cibik, P. Müller, *et al.*, *X-ray pencil beam facility for optics characterization,* (San Diego, California, USA, 2010) p. 77324O.

[21] M. D. Ackermann, M. J. Collon, R. Guenther, *et al.*, *Performance prediction and measurement of silicon pore optics,* (San Diego, CA, 2009) p. 74371N.

[22] M. Krumrey, P. Müller, L. Cibik, *et al.*, *New x-ray parallel beam facility XPBF 2.0 for the characterization of silicon pore optics,* (Edinburgh, United Kingdom, 2016) p. 99055N.

[23] G. Vacanti, N. Barrière, M. Bavdaz, *et al.*, *Measuring silicon pore optics,* in *Optics for EUV, X-Ray, and Gamma-Ray Astronomy VIII*, Vol. 10399, edited by S. L. O'Dell and G. Pareschi, International Society for Optics and Photonics (SPIE, 2017) pp. 131 – 136.

[24] D. Girou, E. Ford, C. Wade, *et al.*, *Design and modeling of a laue lens for radiation therapy with hard x-ray photons,* Physics in Medicine & Biology **66**, 245007 (2021).

3

PLASMA ETCHING FOR THE COMPATIBILITY OF THIN FILM METALLIC COATINGS AND DIRECT BONDING OF SILICON PORE OPTICS

Silicon pore optics are a new type of high-performance X-ray optics designed to enable future space-borne X-ray observatories such as ESA's Athena. These optics will make it possible to build telescopes with effective areas of the order of a few square meters and angular resolutions better than 5 seconds of arc. During manufacturing of the optics, thin film metallic coatings are sputtered onto mirror plates to help achieve this large effective area. Then these plates are stacked on top of each other using direct silicon bonding to achieve the shape of an approximate Wolter type-I telescope design. It is therefore necessary to verify the compatibility of the coating and bonding processes. We observe the unintentional removal of coatings on silicon pore optics plates after their wet chemical activation, a step required to make direct bonding possible. In this chapter we investigate plasma etching prior to thin film deposition as a solution to this problem. First we ensure that plasma etching does not impact the low surface roughness required to achieve high imaging performance. Then we demonstrate that plasma etching before thin film deposition prevents unintentional removal of the metallic coatings during the activation step, making coating deposition compatible with direct bonding of silicon pore optics plates.

Parts of this chapter have been published in the Journal of Applied Physics **128**, 095302 (2020) [1].

3.1 Introduction

As the development of SPO progresses, it is necessary to validate the direct bonding process with the metallic coating deposition process needed for the observatory to achieve a large effective area [2]. The coating deposition process consists in sputtering thin films of metals onto the non-ribbed side of an SPO plate while a patterned photoresist layer prevents the coating from depositing onto the bonding surfaces. The photoresist is then lifted off chemically and the bonding surfaces are cleaned using an RCA recipe [3] (SC-1 cleaning only). Previous studies observed unintentional removal of metallic thin films on SPO after the wet chemical cleaning step required for the direct bonding and indicated that molecular contamination originating from the ambient as well as from fabrication processes such as photoresist remnants might be the cause [4]. Surface treatment is therefore considered to provide clean surfaces prior to thin film deposition and reduce coating surface defects. An inverse sputter etcher (ISE) unit has been implemented in the DC magnetron sputtering machine dedicated for the SPO production [5]. After photoresist deposition this ISE allows for plasma cleaning of the substrate surfaces in situ, before thin film deposition. This way, vacuum is maintained between the plasma etching and coating processes, preventing the substrates to be exposed to the atmosphere. The etching process is performed by bombarding the SPO plate surface with a mixture of argon and oxygen ions. Possible organic contamination and photoresist residuals are removed either by elastic scattering or chemical reactions. However, a potential downside of the process can be an increase in surface roughness by surface modification due to the ion bombardment[6, 7].

In this chapter, we present the results of a study on the effect of plasma etching on SPO plates. We first investigated the possible change in surface roughness with atomic force microscope (AFM) measurements of the plasma etched surfaces. Then we derived the most suitable plasma etching parameters on SPO plates without a photoresist layer. Finally we validated the plasma etching within the coating process on SPO plates with photoresist and proved that it is now compatible with the subsequent bonding step.

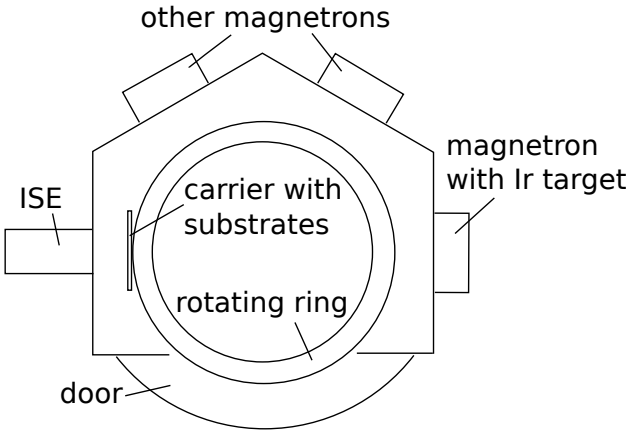
3.2 Evaluating the impact of plasma etching on surface roughness

SPO plate surfaces must have a low root-mean-square (rms) roughness (less than approximatively 0.5 nm) to achieve high imaging performance [8–10]. Therefore the first objective is to ensure plasma etching does not increase the surface rms roughness by surface modification due to ion bombardment. For this purpose we performed AFM measurements on nine non-patterned (without photoresist) SPO plates before and after the plasma etching process.

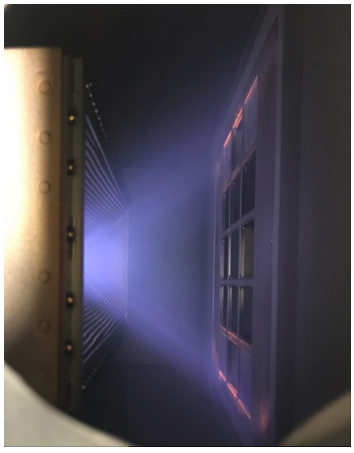
For the plasma etching, the substrates were mounted onto carriers in the coating chamber, as illustrated in Figure 3.1, and exposed to ion bombardment with a mixture of argon and oxygen ions. The plasma discharge power and exposure time vary per sub-

strate and are given in Table 3.1 along with the substrate identification string (id) and the measured rms surface roughness.

AFM measurements were performed in the center of each substrate with scan sizes $1 \times 1\ \mu m^2$ and $20 \times 20\ \mu m^2$. The results obtained are reported in Table 3.1 and show that the rms roughness has decreased, but the change is not significant: 0.25 ± 0.03 nm before plasma etching versus 0.22 ± 0.01 nm after. Plasma etching intensity also has no significant effect on the rms roughness with current condition.



(a)



(b)

Figure 3.1: Views of the coating chamber from above. (a) Schematic view displaying the position of the inverse sputter etcher (ISE) compared to the Iridium target and its magnetron. The carriers holding the substrates are mounted on a rotating ring passing by the ISE and the Iridium target successively. Note that two additional magnetrons are available in the chamber and that a door is used to load and unload the carriers. (b) Discharge plasma glow of the ISE. The ISE is visible on the left of the picture and the carriers with the substrates on the right.

Table 3.1: AFM results of nine non-patterned, non-coated SPO plates before and after plasma etching. The plasma discharge power and exposure time vary per substrate. The AFM measurements were performed in the center of each substrates with scan sizes $1 \times 1\ \mu m^2$ and $20 \times 20\ \mu m^2$, respectively.

Substrate id	Discharge power (W)	Exposure time (s)	rms before plasma (nm) $1 \times 1\ \mu m^2$	rms before plasma (nm) $20 \times 20\ \mu m^2$	rms after plasma (nm) $1 \times 1\ \mu m^2$	rms after plasma (nm) $20 \times 20\ \mu m^2$
532-10	100	120	0.25	0.20	0.24	0.19
537-10	100	240	0.25	0.21	0.23	0.20
590-12	100	360	0.28	0.21	0.23	0.21
590-13	450	120	0.29	0.27	0.24	0.21
548-10	450	240	0.25	0.23	0.22	0.21
635-06	450	360	0.25	0.22	0.23	0.22
638-02	800	120	0.27	0.24	0.21	0.22
692-12	800	240	0.26	0.23	0.23	0.23
638-15	800	360	0.28	0.27	0.23	0.24

3.3 Investigating coating stability on non-patterned SPO plates

A 10.0-nm thick Iridium layer (Table 3.2) was deposited on two non-patterned (that is without photoresist), non-plasma-etched SPO plates (substrates 714-10 and 714-11) as well as four non-patterned, plasma-etched SPO plates (substrates 714-01, 714-05, 714-07 and 714-08). The substrates underwent plasma etching with powers 100 W and 450 W, and were thereafter subjected to a wet chemical process (SC-1 cleaning) needed for direct bonding of plates in the complete SPO manufacturing process.

To determine if any damage to the Iridium film occurred during the SC-1 clean, we took two sets of images with an optical microscope, one right after the Iridium deposition and another after the SC-1 clean. The optical microscope images are presented in Figure 3.2. The plasma etching effect is noticeable after the SC-1 clean. Indeed, for the non-plasma etched substrates (i.e. substrate 714-10) numerous holes appear in the Iridium film after the SC-1 clean. The SPO plates plasma etched with a discharge power of 100 W (i.e. substrate 714-01) show an improvement (fewer holes). At a discharge power of 450 W (i.e. substrate 714-07), the plasma etching proved effective at preventing holes in the Iridium film after the SC-1 clean. Note that the holes have a higher density at the edges of the plates.

Results of AFM measurements on the substrates are reported in Table 3.3. The rms roughness of the sputtered Iridium film on non-plasma-etched SPO plates (substrates 714-10 and 714-11, 0.25 ± 0.03 nm) is not significantly different from the rms roughness of the sputtered Iridium film on plasma-etched SPO plates (714-01, 714-05, 714-07 and 714-08, 0.24 ± 0.01 nm).

To assess the impact of SC-1 cleaning on the Iridium coating thickness we also per-

formed X-ray reflectivity (XRR) measurements at 8 keV on the center of the substrates, where the hole density is low for all SPO plates. The data and the best fit models are shown in Figure 3.3, and the best fit thicknesses and roughness are reported in Table 3.3. For the different plasma etching parameters, no significant difference in rms roughness nor thickness of the Iridium films is observed.

We conclude that the thickness and the rms roughness of the sputtered Iridium thin film is not impacted by plasma etching of the non-patterned SPO plates. Plasma etching does however affect the resistance of the coating to SC-1 cleaning, with the higher discharge power of 450 W yielding better results. The higher density of holes at the edges of the plates is attributed to handling of the mirror plates prior to coating; the plates are held on their edges, resulting in possible organic contamination in these areas.

Table 3.2: Parameters for the sputter deposition of 10 nm of Iridium.

Maximum base pressure	2.0×10^{-6} mbar
Working gas pressure	3.4×10^{-3} mbar
Power density	3.1 W cm^{-2}
Target-to-substrate distance	105.0 mm

Table 3.3: AFM and XRR results of two non-plasma-etched SPO plates (substrates 714-10 and 714-11) as well as four plasma etched SPO plates (substrates 714-01, 714-05, 714-07 and 714-08). All substrates are non-patterned, coated with 10 nm of Iridium and have gone through an SC-1 clean. No significant difference in rms roughness nor thickness of the Iridium films is observed.

Substrate id	Discharge power (W)	Exposure time (s)	rms after Iridium coating (nm) 1×1 μm^2	rms after Iridium coating (nm) 20×20 μm^2	XRR fitted thickness (nm)	XRR fitted rms roughness (nm)
714-10	-	-	0.27	0.23	10.1	0.29
714-11	-	-	0.28	0.23	-	-
714-01	100	120	0.24	0.24	10.2	0.29
714-05	100	120	0.25	0.23	-	-
714-07	450	120	0.25	0.23	10.2	0.32
714-08	450	120	0.25	0.24	-	-

3.4 Validating coating stability on patterned SPO plates

The complete SPO manufacturing process includes coating deposition by sputtering thin films of metals onto the non-ribbed side while a photoresist layer prevents the coating from depositing onto the bonding surfaces, enabling direct silicon bonding. This photoresist has a pattern matching the ribs on the backside of the plate (see Figure 3.4). The photoresist is lifted-off chemically in a dimethyl sulfoxide (DMSO) bath after coating deposition and before SC-1 clean.

A layer of 10.0 nm of Iridium was deposited on two patterned (with photoresist), non-plasma-etched SPO plates (substrates 10000-16 and 10005-15) as well as seven pat-



(a)

(b)

(c)

Figure 3.2: Optical microscope images (magnification x5) of substrate corners. Each image shows about 1 mm in the vertical direction and 1.5 mm in the horizontal direction out of the 40.0×65.7 mm^2 substrate surfaces. (a) Substrate 714-10, without plasma etching, (b) substrate 714-01, etched with 100 W and (c) substrate 714-07, etched with 450 W. **Left**, before SC-1 cleaning. **Right**, after SC-1 cleaning. All substrates are non-patterned and coated with 10 nm of Iridium. Fewer holes appear in the Iridium film after the SC-1 clean as the discharge power increases.

terned, plasma-etched SPO plates (substrates 10008-04, 10008-05, 10008-07, 10008-12, 10008-06, 10002-12 and 10008-15). The discharge power of the plasma was 450 W and the exposure time 240 seconds. Subsequently, all substrates went through a lift-off process and then to the SC-1 clean.

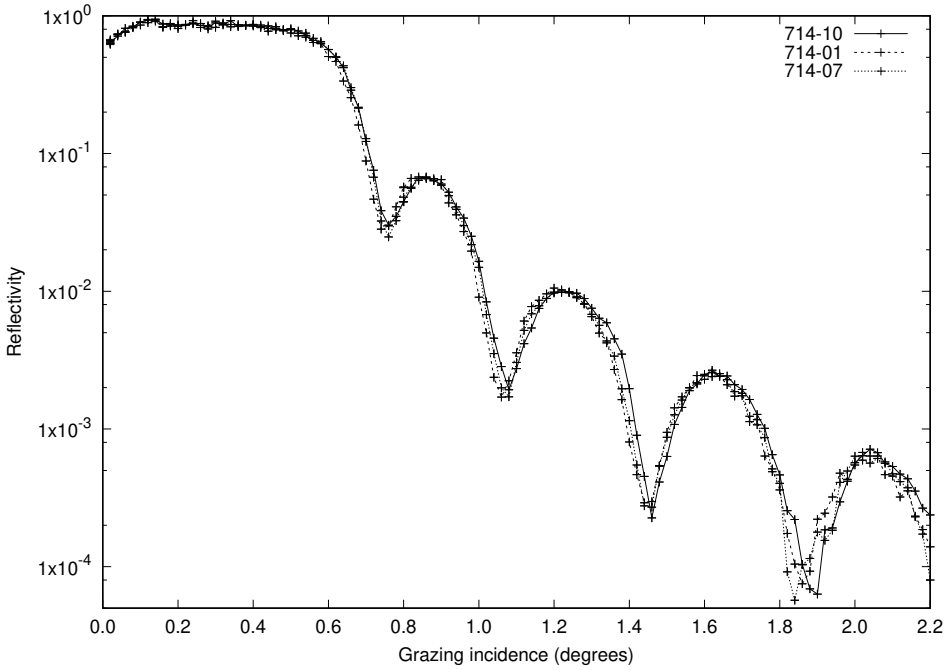


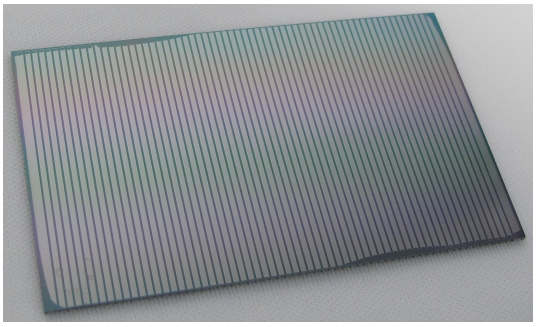
Figure 3.3: Measured XRR of three SPO plates: substrate 714-10 (non-plasma etched), substrate 714-01 (etched with 100 W) and 714-07 (etched with 450 W). All substrates are non-patterned, coated with 10 nm of Iridium and have gone through an SC-1 clean. The rms roughness and thickness of the Iridium films are not significantly different for the different plasma etching powers, resulting in similar XRR.

Figures 3.4 and 3.5 show substrates 10005-15 (without plasma etching) and 10008-04 (with plasma etching) after lift-off (before the SC-1 clean) and after SC-1 cleaning. The Iridium coating has been unintentionally removed on most of the surface of substrate 10005-15 which did not undergo plasma etching (see Figure 3.4). This observation indicates the presence of residual photoresist on the entirety of the reflective side of the patterned SPO plate prior to coating deposition as seen in a previous study[4]. However, the Iridium coating is still present on substrate 10008-04 which underwent plasma etching (see Figure 3.5), indicating that photoresist has been etched by the plasma prior to coating deposition.

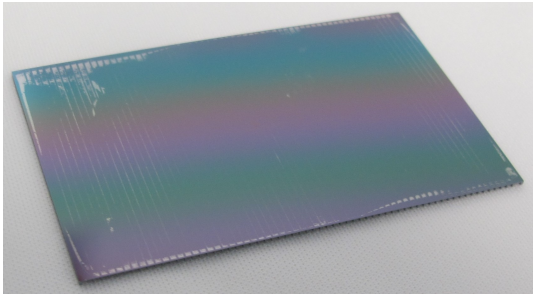
In both cases though (with or without plasma etching), the Iridium coating has been unintentionally removed along the edges of the reflective side of the substrates directly after lift-off. The pattern of this coating removal (edges only) supports the hypothesis that photoresist residuals are present in these areas even after plasma etching.

There the resist might be thicker due to edge effects during deposition by spin coating; thickness distribution should be examined and other improved coating method such as spray coating should be considered.

Figure 3.6 shows optical microscope images (magnification x5) of the center of substrate 10008-04 which underwent plasma etching. The interfaces between Iridium coating and silicon oxide are sharp and no holes in the coating are observed. If present, the photoresist residuals on the coating areas (between the patterned stripes) have been etched away by the plasma prior to coating deposition.



(a)

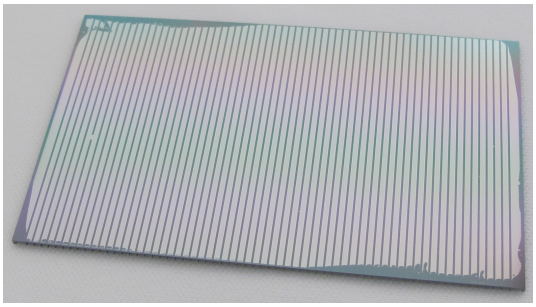


(b)

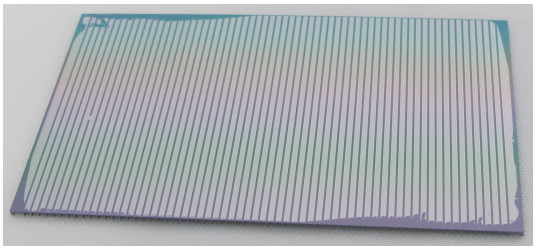
Figure 3.4: Substrate 10005-15 (without plasma etching). Substrate dimensions are about $40.0 \times 65.7 \times 0.8\ mm^3$. (a) After lift-off, (b) after SC-1 cleaning. The Iridium coating has been unintentionally removed on most of the substrate surface.

3.5 Conclusions and discussion

Plasma etching of SPO plate surfaces before thin film deposition prevents unintentional removal of the metallic coatings during SC-1 cleaning. This indicates that the substrates have photoresist residuals and/or organic contamination on the reflective side. Indeed the plasma etching process performed by bombarding the SPO plate surface with a mixture of argon and oxygen ions would remove, if present, photoresist residuals and organic contamination by elastic scattering and/or chemical reactions. Most of the organic contamination and some of these residuals have been removed successfully by plasma etching with a discharge power of 450 W prior to coating deposition but not in the regions close to the edges. There, photoresist residuals might be thicker due to the spin



(a)



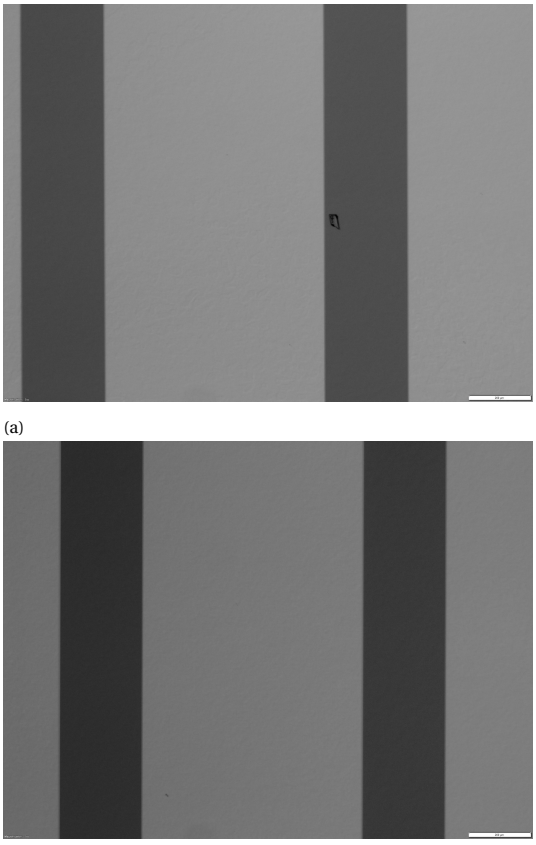
(b)

Figure 3.5: Substrate 10008-04 (with plasma etching). Substrate dimensions are about $40.0 \times 65.7 \times 0.8$ mm^3. (a) After lift-off, (b) after SC-1 cleaning. The Iridium coating is unaffected by the SC-1 clean based on visual inspection.

coating deposition method used. We recommend to measure the thickness distribution of the photoresist layer and to consider spray coating. Also, it would be interesting to perform direct measurement of the organic contamination, for instance by using X-ray photoelectron spectroscopy.

It is also concluded that plasma etching and thin film deposition do not impact the surface rms roughness, allowing for low scattering and high imaging performance from the coated SPO plates.

Overall, this work demonstrates that plasma etching makes the metallic coating deposition process compatible with the SC-1 cleaning step needed for direct silicon bonding. This is essential to increase the effective area of SPO-based X-ray telescopes like Athena, to build complex shapes such as Wolter type-I that will survive launch and space flight conditions, and therefore to extend the breadth and scope of future astrophysical observations.



(a)

(b)

Figure 3.6: Optical microscope images (magnification x5) of the surface of substrate 10008-04 (with plasma etching). (a) After lift-off, (b) after SC-1 cleaning. In both cases the interfaces between Iridium coating (light grey) and silicon oxide (dark grey, 270 μm in the horizontal direction) are sharp and no holes are observed in the coating.

References

[1] D. Girou, S. Massahi, D. D. M. Ferreira, *et al.*, *Plasma etching for the compatibility of thin film metallic coatings and direct bonding of silicon pore optics,* Journal of Applied Physics **128**, 095302 (2020), https://doi.org/10.1063/5.0010212 .

[2] D. D. M. Ferreira, F. E. Christensen, A. C. Jakobsen, *et al.*, *ATHENA optimized coating design,* in *Space Telescopes and Instrumentation 2012: Ultraviolet to Gamma Ray*, Vol. 8443, edited by T. Takahashi, S. S. Murray, and J.-W. A. den Herder, International Society for Optics and Photonics (SPIE, 2012) pp. 1601 – 1611.

[3] W. KERN, *Cleaning solutions based on hydrogen peroxide for use in silicon semiconductor technology,* RCA Review **31**, 187 (1970).

[4] S. Massahi, D. A. Girou, D. D. M. Ferreira, *et al.*, *Investigation of photolithography process on SPOs for the Athena mission,* in *Optics for EUV, X-Ray, and Gamma-Ray Astronomy VII*, Vol. 9603, edited by S. L. O'Dell and G. Pareschi, International Society for Optics and Photonics (SPIE, 2015) pp. 155 – 165.

[5] S. Massahi, F. E. Christensen, D. D. M. Ferreira, *et al.*, *Installation and commissioning of the silicon pore optics coating facility for the ATHENA mission,* in *Optics for EUV, X-Ray, and Gamma-Ray Astronomy IX*, Vol. 11119, edited by S. L. O'Dell and G. Pareschi, International Society for Optics and Photonics (SPIE, 2019) pp. 91 – 106.

[6] S. C. Vitkavage and E. A. Irene, *Electrical and ellipsometric characterization of the removal of silicon surface damage and contamination resulting from ion beam and plasma processing,* Journal of Applied Physics **64**, 1983 (1988).

[7] R. Pétri, P. Brault, O. Vatel, *et al.*, *Silicon roughness induced by plasma etching,* Journal of Applied Physics **75**, 7498 (1994).

[8] J. Stover, *Optical Scattering: Measurement and Analysis*, Press Monographs (SPIE Press, 2012).

[9] D. Spiga, G. Cusumano, and G. Pareschi, *HEW simulations and quantification of the microroughness requirements for x-ray telescopes by means of numerical and analytical methods,* in *Optics for EUV, X-Ray, and Gamma-Ray Astronomy III*, Vol. 6688, edited by S. L. O'Dell and G. Pareschi (SPIE, 2007) p. 66880H.

[10] D. Spiga, *Optical module HEW simulations for the X-ray telescopes SIMBOL-X, EDGE and XEUS,* in *Optics for EUV, X-Ray, and Gamma-Ray Astronomy III*, Vol. 6688, edited by S. L. O'Dell and G. Pareschi (SPIE, 2007) p. 66880K.

4

DESIGN AND MODELING OF A LAUE LENS FOR RADIATION THERAPY WITH HARD X-RAY PHOTONS

We have designed and modeled a novel optical system composed of a Laue lens coupled to an X-ray tube that produces a focused beam in an energy range near 100 keV ($\lambda = 12.4$ picometer). One application of this system is radiation therapy where it could enable treatment units that are considerably simpler and lower in cost than present technologies relying on linear accelerators. The Laue lens is made of Silicon Laue Components (SiLCs) which exploit the Silicon Pore Optics (SPO) technology. The lens concentrates photons to a small region thus allowing high dose rates at the focal area with very much lower dose rates at the skin and superficial regions. Monte Carlo simulations with Geant4 indicate a dose deposition rate of 0.2 Gy/min in a cylindrical volume of 0.7 mm diameter and 10 mm length, and a dose ratio of 72 at the surface (skin) compared to the focus placed 10 cm within a water phantom. Work is ongoing to newer generation crystal technologies to increase dose rate.

Parts of this chapter have been published in Physics in Medicine & Biology **66**, (2021) 245007 [1].

4.1 Introduction

Radiation therapy plays an essential role in the treatment of cancer, with more than 60% of patients receiving radiation therapy, mainly in the form of high-energy photons (2-20 MeV), in the course of their disease management [2]. Such high-energy photons present many challenges due to their penetrating power and the ionisation damage they cause to healthy, as well as diseased, tissue [3]. The technology used in radiation therapy for cancer treatment can be used to exquisitely shape the radiation dose around a tumour inside a patient with a precision that is an order-of-magnitude better than twenty years ago. However, some tumors are still not curable. New approaches are being explored such as using radiation in combination with targeted agents such as immune-modulating drugs [4]. While radiation therapy as a single-agent for cancer treatment may have reached the limits of its achievements, this modality is likely to be needed in the long term. As such, technology development efforts are well-justified [5].

Radiotherapy uses ionizing radiation to damage the DNA of cancerous tissue causing cellular death and slowing cell growth. In external beam therapy the radiation beam enters the patient on the surface, delivering a superficial dose D_S. Beneath the surface, the dose first rises rapidly with depth, reaching a maximum value at a depth $d_{\max}$, and then decreases almost exponentially until it reaches an exit dose value at the patient's exit point[6]. The relatively low surface dose for high-energy photon beams (referred to as the skin-sparing effect) is of great importance in radiotherapy to treat deep-seated lesions without undue toxicity to the skin and superficial tissues. The tumor dose can be concentrated at deep depths in the patient while delivering a relatively low dose to the skin and other normal tissues at superficial depths which are not involved in the disease. The dose region between the surface and the depth of dose maximum $d_{\max}$ is called the dose buildup region and represents the region in the patient in which the dose deposition rises with depth as a result of the range of secondary electrons released in tissue by photon interactions with the atoms of tissue. It is these secondary electrons released by photons that deposit energy in tissue (indirect ionization). The greater the photon energy, the more extensive the range of secondary electrons and, consequently, the larger the depth of dose maximum. These considerations have led to the almost exclusive use of MeV photon beams for radiotherapy.

However, the ability to deliver therapeutic treatments with low-energy radiation (< 200 keV) would be attractive for several reasons. First, one could envision more cost-effective treatment units compared to the linear accelerator technologies currently required to create a high-fluence beam of tens of MeV energy. More reliable, cost-effective solutions are especially attractive as cancer therapy needs expand in low- and middle-income countries which in some cases lack even a single treatment facility due to technology and cost barriers [2].

Therapy beams at low energies may also be attractive in their ability to achieve increased sensitivity when used in combination with high-Z nanoparticles. Recent high-profile studies have shown that tumor cell survival is significantly reduced by combining

X-ray irradiation with gold nanoparticles [7]. This reduction is due to dose enhancement in or near the cell, which results from photoelectric effects in the high-Z nanoparticle [8]. A large dose enhancement factor (66%) was observed for low energy X-rays (< 200 keV). However, as described in the previous paragraph, it is not currently possible to deliver low-energy irradiation in the clinical setting without unacceptable toxicity to the skin and normal tissue. Medical physicists have therefore altered their approach [9] and are now considering gold nanoparticles in combination with the high-energy beams which are routinely used in the clinic (mean energy ~2 MeV). However, at these energies the photoelectric interactions are orders of magnitude lower [8] and therefore have a dose enhancement of only 10-20% [7]. In summary, low-energy radiation (< 200 keV) combined with high-Z nanoparticles would be extremely effective against tumor cells. However, it is not currently possible to deliver low-energy radiation to deep-seated tumors in a patient.

In this chapter, we report a possible solution to create a converging beam, which spares the skin by spreading the dose over a large area. This is similar to the concept reported by Breitkreutz et al. [10] and references therein but instead of using a mechanical system with multiple sources and collimation, the present study uses an X-ray lens system. This is also different from polycapillary optics which work at lower energy and can thus not be used for deep seated tumors [11]. This is an update of work from our group presented by Wade et al. [12] where we investigated lens designs and assembly techniques. In the current chapter, we first describe how silicon pore optics (SPO) technology can be used to create self-focusing Laue lens elements, the so-called Silicon Laue Components (SiLCs). Then, we detail the method used to design such SiLCs, including the in-house Monte-Carlo SiLC Simulation Code (SSC) we developed to simulate diffraction in SiLCs. Finally, we present the optimized lens design and show that this lens can provide an unprecedented ratio of dose at the surface (skin) compared to its focus, based on Geant4[13–15] simulations. Note that while obtaining different results (see Section 4.4.3), the effort and methods detailed in this chapter can be compared to the work of Paternò[16] and Camattari [17].

4.2 Silicon Laue components

A Laue lens is a concentrator that uses Bragg diffraction in the volume of symmetrically cut crystals (referred to as Laue geometry). Laue lenses are an emerging technology based on crystal diffraction that enables soft gamma-ray focusing. Laue lenses have the potential to overcome the limitations imposed by the depth dose distribution, thereby enabling the clinical use of low-energy photon beams for radiotherapy. In high-energy astrophysics, there have been significant efforts devoted to the development of a focusing gamma-ray technology [18–24].

Diffraction lenses use the interference between the periodic nature of the electromagnetic radiation and a periodic structure such as the matter in a crystal. In order to

be diffracted, an incoming gamma-ray must satisfy the Bragg condition:

$$2d_{hkl}\sin\theta = n\frac{hc}{E} \tag{4.1}$$

where d_{hkl} (in Å) is the spacing of the lattice planes (hkl), n is the diffraction order, h is the Planck constant, c is the speed of light, and E is the energy of the gamma-ray photon.

In the transmission configuration, a Laue lens is made of many individual crystals that are arranged so that they will all diffract the incident radiation onto a common focal spot. For a given set of planes and order of reflection, the Bragg condition is only met for a single energy. Mosaic crystals or curved crystals can be used to increase the bandpass. Mosaic crystals can be modeled as an assembly of perfect microscopic crystals (crystallites) whose lattice planes are slightly misaligned with each other around a mean direction, following a normal distribution[25]. Similarly, curved crystals have an angular dispersion of the lattice planes and a larger energy passband than perfect crystals. Though the downside is mosaic defocusing, i.e. the fact that the energy bandpass comes from a range of angular crystal plane orientation, but also results in a range of directions for the diffracted rays as a function of their wavelength. Curved crystals can be obtained in various ways, including the elastic bending of a perfect crystal[26] (the technique commonly used in synchrotron radiation facilities), or the growing of a two-component crystal[27, 28] whose composition varies along the crystal growth axis, or the indentation of one face of a wafer[29].

The diffracted flux from a continuum source increases with increasing mosaicity of mosaic crystals or the total bending angle of curved crystals[25]. For a Laue-lens telescope, crystals with mosaicities or total bending angles ranging from a few tens of arcseconds to a few arcminutes are relevant. The bandwidth of a lens for an on-axis source is determined by the mosaicity or total bending angle of the individual crystals and by the accuracy of the alignment of the single crystals. The rectangular diffraction profiles of curved crystals produce more effective flux concentration than the Gaussian profiles of mosaic crystals [30]. Curved crystals have higher peak diffraction efficiency (100% max.) than mosaic crystals (50% max.) due to the absence of extinction effects[31]. However, Laue lenses constructed from either mosaic or curved crystals have several limitations. For instance, the smallest spot size that can be achieved is given by the size of the smallest crystal element in the lens. Also, the individual components of the lens are not focusing elements themselves. Furthermore, the assembly of the lens relies heavily on the accurate placing of many hundreds (or thousands) of crystal elements, which is challenging.

Laue-lens technology has been slowly developing for several decades[12, 21, 22, 32] and recently took a new turn with Silicon Laue Components (SiLCs)[33] based on silicon pore optics technology. Silicon pore optics (SPO) are a new type of X-ray optics designed to enable future space-borne X-ray observatories such as Athena [34]. Since X-rays from celestial sources do not penetrate Earth's atmosphere, X-ray telescopes must be in space. SPO are being developed by the European Space Agency (ESA) in collaboration with academic and industrial partners [35, 36]. These high-performance, modular,

lightweight yet stiff, high-resolution X-ray optics shall allow space telescopes to reach an unprecedentedly large effective area of a few square meters, operating in the 0.2 to 12 keV band with an angular resolution aiming at being better than 5 arcseconds. To this end, custom-made assembly tools and processes have been developed to build SPO using direct silicon bonding[37, 38]. Because each SPO plate is a single side ribbed rectangular silicon substrate, stacking them results in a pore-like structure. X-ray photons enter these pores at low grazing angles, are reflected on the top side of each plate inside the pores, and exit the optics at the opposite end.

SPO technology can also be used to fabricate soft gamma-ray Laue lenses if Bragg diffraction through the bulk silicon is exploited, rather than grazing incidence reflection. A SiLC-based Laue lens can focus photons in the range ~80 keV to ~300 keV, and present several advantages over alternative Laue lens concepts. SiLCs are made of stacks of curved, polished, wedged silicon plates, and contrary to SPO, the individual plates are not ribbed. Each element is bent in two dimensions, with a meridional and a sagittal curvature. The direction of sagittal curvature is perpendicular to the optical axis, ensuring the normal vector to the plate's surface always points at the optical axis, which allows for X-rays to be reflected to a common focus. Therefore the sagittal curvature of each plate is part of a circle centered on the optical axis. The meridional curvature is in a plane that encompasses the optical axis. In the case of SPO, where the source is at infinity, all the incident rays are parallel, and the meridional curvature will create a variation of the angle of incidence onto each plate as a function of the position along the optical axis. For SiLCs, the meridional curvature creates an angular bandpass or angular width for each crystal, similar to mosaicity. When the source is not at infinity, even a plate which does not have any meridional curvature is seen by the source as a range of angles: this is simply the angle subtended by the plate. Meridional curvature can be designed to match with this angle such that the rays diffracted at any point along the axis will be focused to a common point. This will also lead to a nearly monochromatic bandpass for each given plate. The sagittal and meridional curvatures lead to significantly improved focusing, which reduces the size of the point spread function (PSF) of the lens compared to unbent diffracting crystals. Indeed the size of the focal spot is no longer determined by the size of the individual single crystals but by the accuracy of the applied curvatures. This property leads to considerably higher signal to noise ratios than what is achievable with a conventional Laue lens design made of mosaic crystal tiles. Another distinct advantage is the reproducible quality of the materials which are compatible with large-scale production. The SiLCs are made of diced silicon wafers, which are commercially available with well-defined quality (i.e. purity, surface roughness and total thickness variations). An illustration of a SiLC is shown in Figure 4.1.

Since the plates composing SiLCs are bent following arcs of circles, SiLCs can be used to populate concentric rings, whose center defines the optical axis. An example of this is shown in Figure 4.2 where a full lens is displayed in the plane perpendicular to the optical axis. The optical axis runs through the center of the lens. Each SiLC has an inner and outer radius, which are related by the number of plates and their thickness. Multiple rings of SiLCs are present in this example.

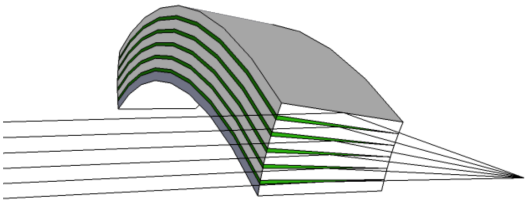


Figure 4.1: Illustration of a SiLC. The lines represent photons trajectories going from left to right. The green part represents the wedge (not to scale).

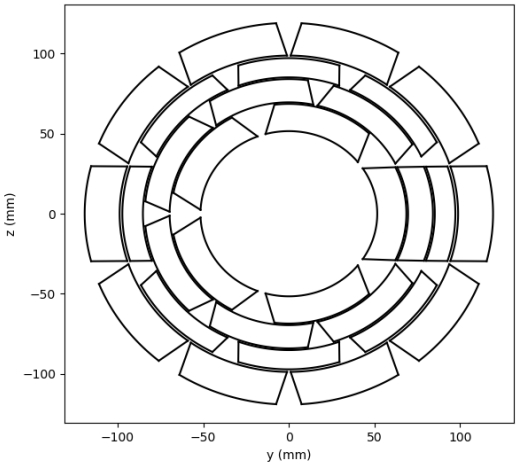


Figure 4.2: Example of a full lens consisting of multiple SiLCs in the y-z plane (plane perpendicular to the optical axis). The optical axis (x-axis) runs through the center of the lens.

4.3 Lens design method

4.3.1 System parameters

It is useful to describe the geometry of the system in terms of the distance d between the source and lens, the distance f between the lens and focus, and the distance r of a plate to the optical axis. These distances are schematically shown in Figure 4.3.

For fixed values of d, f, and r, the angle a plate makes with respect to the optical axis is fixed. Assuming the crystal planes are in the same plane as the plate surface, then d_{hkl} is known and the Bragg angle θ_{Bragg} can be determined by Equation 4.2 and can be used to calculate the energy reflected at the center of the plate by using Equation 4.1.

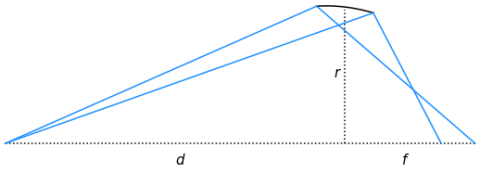


Figure 4.3: Schematic of the side view geometry of the system. It shows the three relevant distances d, f and r and how they translate to the angle a plate makes with the optical axis. Note that the meridional curvature of a plate is represented here as well.

$$\theta_{\text{Bragg}} = \frac{\pi - \arctan\left(\frac{d}{r}\right) - \arctan\left(\frac{f}{r}\right)}{2} \tag{4.2}$$

However, as plates are stacked on top of each other, the center of each plate will be at a different distance r from the optical axis and, therefore, also makes a different angle with the optical axis. Therefore each plate is given a wedge so that the plate on top of it also has the desired orientation. We thereby define two new system parameters, the initial angle or the angle the bottom plate of a SiLC makes with the optical axis, and the wedge or the average wedge required to get all other plates in the right orientation.

The center of each plate in the SiLC will reflect a different energy, thus contributing to the energy bandpass of the lens. Additionally, each plate also has a bandpass determined by the Bragg angle corresponding to the front and the back of the plate (as seen from the source). This bandpass can be controlled by the length of the plate and its meridional curvature, which is the difference in orientation of the crystal planes between the front and the back of a plate. The method of determining the optimal plate length and meridional curvature is described in Section 4.4.

4.3.2 System constraints

In the lens design presented in this chapter, three different system constraints are being considered: the minimal radius, the minimal convergence angle, and the minimal energy. First, there is a physical limit to the elastic bending of silicon plates. If a certain curvature threshold is crossed, the plates will break. The bonding energy needs to be strong enough to counteract the spring force from the bent plates. For these reasons, a limit must be set on the radius r of the inner-most plate. Second, two factors of significant influence on the dose delivered to the skin are the convergence angle of the reflected X-rays and the energy of these X-rays. The convergence angle is defined as the angle between the diffracted rays and the optical axis. Finally, as the diffracted energy decreases with increasing r, the constraint of a minimal reflected energy E_{min} can be translated to a maximum allowable radius r_{max} of a plate by solving Equation 4.2 for r.

The constraints on the minimum radius, maximum radius, and convergence angle are shown graphically in Figure 4.4, for a fixed source to focus distance $d + f = 4$ m, as the horizontal line, curved line, and tilted line, respectively. All plates of the SiLC must then fall within the area highlighted in blue.

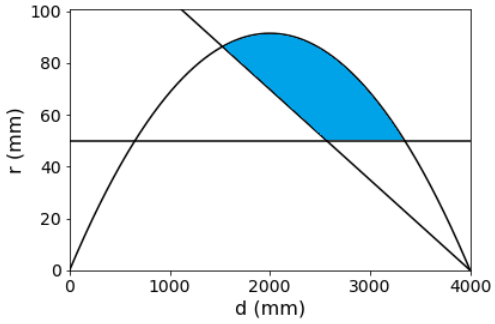


Figure 4.4: Schematic representation of the system constraints. The minimum radius (horizontal line), minimum convergence angle (tilted line), and radius of minimum reflected energy (curved line) constrain the plates in a SiLC to all fall within the blue area.

4.3.3 Dimensions and shape of the focus

It is essential to distinguish between the desired focal spot of the combination of all plates and the focal spot of a single plate. The initial angle and wedge of the plates will determine the position of the general focal spot, while the meridional curvature of a plate determines the position of its meridional focus. These two do not have to be in the same position in space. Moreover, as tumors are three-dimensional objects, it is crucial to consider the focal spot in three dimensions. Therefore, it is chosen to take a value of the meridional curvature that focuses the X-rays before the desired focus. This choice creates the desired effect of extending the focus in the optical axis direction while simultaneously slightly increasing the meridional curvature, thus increasing the diffracted flux. From this geometry, we can define a value for the angular width as the difference between the angle the left and right side of the plate (as displayed in Figure 4.3). This approach leads to a relation between the meridional curvature and the plate length based on geometric considerations and not based on optimizing the reflectivity.

In this chapter, it is chosen to find an optimized combination of angular width and plate length numerically for a given configuration. For application in radiation therapy, it is deemed more useful to deliver the maximum dose to the focal point rather than increasing the reflectivity and thereby also increasing the dose delivered to unwanted areas. Contrary to the sketch in Figure 4.3, the rays do not stop at the focus, but rather keep going. The focus is thus 3-dimensional, defined by the volume of highest dose deposition.

4.3.4 Energy versus convergence angle

In our system, there is a trade off between energy diffracted and convergence angle. Indeed, convergence angle can be increased by either increasing the sagittal radius r of the plates, or by bringing the lens closer to the focus (decreasing f). In both cases, the deflection angle increases which results in lower diffracted energy. It is possible to compensate these effects and increase the energy diffracted by using higher diffraction orders, but this comes at the expense of diffracted flux as the reflectivity rapidly decreases with higher order diffractions. Ultimately, the focus-to-skin dose ratio is the parameter that we want to maximize. So we investigate the effect of energy and convergence angle to this parameter to guide the lens design. We used Geant4 to simulate the dose distribution of a beam of mono-energetic X-rays converging to a focal point of 1 mm in diameter placed 10 cm deep within a water phantom, originating from an annulus with 8 and 9 cm inner and outer radius, respectively. The annulus was placed at various distances between 1 m and 3 m from the focus, thereby varying the convergence angle. The energy of the X-rays was varied between 100 keV and 300 keV. From this simulation, we extracted the focus-to-skin dose ratio. The results are shown in Table 4.1, here the lengths have been converted to the corresponding convergence angle.

Table 4.1: Focus-to-skin dose ratio for combinations of X-ray energy and convergence angle.

	100 keV	150 keV	200 keV	250 keV	300 keV
4.85°	12.6	16.1	17.4	20.2	21.0
3.24°	-	8.8	-	10.7	-
2.43°	5.1	5.9	6.9	7.7	8.2
1.95°	-	4.8	-	6.1	-
1.62°	3.3	3.8	4.6	5.1	5.5

The results show that increasing the energy from 100 keV to 300 keV hardly doubles the focus-to-skin dose ratio, while increasing the convergence angle from about 1.6° to about 4.9° almost quadruples this ratio. We conclude that a larger convergence angle should be favored over a large energy, given that it is not possible to have both due to the constraining relation between diffraction angle and energy.

4.3.5 Diffraction orders

Lower diffraction orders result in higher reflectivity, but correspond to a smaller Bragg angle, resulting in a reduced convergence angle. Therefore, the choice of what diffraction order to use becomes a trade-off between reflectivity and convergence angle. As seen in the previous section, a larger convergence delivers higher focus-to-skin dose ratio and should be favored for radiotherapy. Therefore this problem can be dealt with using a simple rule of thumb: maximize the convergence angle using the lowest diffraction order possible.

4.3.6 SiLC reflectivity and spectrum

Assuming the X-ray source to be a point source, the energy diffracted at each point in a plate can be calculated. Figure 4.5 shows a meridional cut through a SiLC made of 100 plates of 170 μm thickness, and each point is colored based on the energy it diffracts.

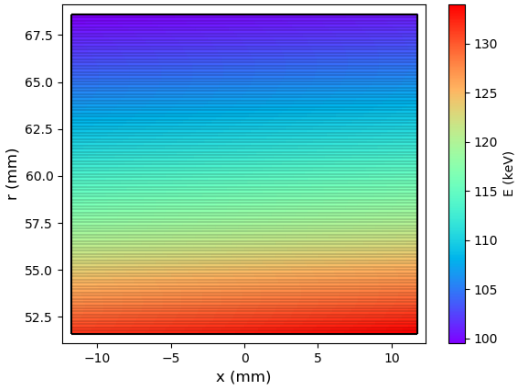


Figure 4.5: Figure of the reflected energy at each point in the SiLC. Each plate has its own bandpass. The average energy diffracted at each plate changes due to the different angle the plate makes with the optical axis and the different radius of each plate.

An approximation of the reflected spectrum of this SiLC can be calculated, assuming most photons enter the SiLC through the side facing the source, rather than through the bottom side facing the optical axis. For this, it is assumed that the incoming spectrum is uniform with an intensity of 1 and that the contribution of each plate to the SiLC spectrum is uniform within its bandpass. Then, within the spectrum, each plate contributes only within the boundaries of its bandpass, and its contribution equals its reflectivity divided by the number of plates in the SiLC. Notice that for the situation where each plate would have an identical bandpass and reflectivity, the spectrum would be uniform with a value of the plate's reflectivity and the plate bandpass width. Figure 4.5 shows that only a few plates will be able to diffract a given X-ray energy. Therefore, if an X-ray of this energy hits the SiLC anywhere, it only has a probability of being diffracted when it hits a plate in which it can diffract. We then define the effective reflectivity as the reflectivity divided by the number of plates in the SiLC. For example, if all plates diffracting a specific X-ray energy have an average reflectivity of 0.2, and 10 out of 100 plates can diffract this energy, then the effective reflectivity for this energy will be 0.02.

4.3.7 SiLC Simulation Code (SSC)

The properties of the design must be well understood to optimize the design for a SiLC lens. To this end, an in-house Monte-Carlo ray trace code named SSC was developed to simulate the output of a given design when illuminated by a source characterized by its

spectrum (e.g., tungsten anode X-ray tube, flat continuum, monochromatic) and spatial extent (e.g. point source, extended disc). The code was validated step by step, starting from the simplest geometry for which analytical calculation is trivial (single flat plate, point source with flat continuum spectrum). The results were then validated for each added level of complexity: plate with curvature, stack of plates, stack of plates with curvature, and finally stack of plates separated by thin wedge. In a lens design, the point spread function (PSF) is affected by many parameters, including the dimensions of the individual plates, the number of plates in a stack, Miller index of diffracting planes, and the radii of meridional curvature. The SSC uses ray-tracing and diffraction physics to facilitate the study and optimization of different lens designs. The code is used to test the spectral and spatial properties of the PSF produced by a lens design when illuminated by a given source. The code generates photons with randomized origins (for an extended source), directions, and energies based on distributions defined by a particular source such as an X-ray generator for simulating testing conditions. Ray-tracing is used to calculate which plates a given photon interacts with and the entrance and exit points of the photon for each of those plates. Since the plates are bent in two directions (sagittal and meridional), the normal of the diffracting plane changes along a photon's path through a plate. This change complicates the calculations estimating the probability of different interactions the photon may have (transmission, diffraction, or absorption). To calculate the probability of these interactions, the model for distorted crystals described by Malgrange[39] is used. If diffraction occurs, a new photon is generated, and its path through the lens is measured to test for multiple reflections. When photons are first generated, they are given an intensity of 1. As reflections occur, the intensity is appropriately decreased. Put another way, the code calculates the possible positions where an incoming photon can undergo diffraction and the subsequent direction of travel. The intensity values assigned to a photon reflect the probability of it exiting the lens in that particular state (coordinate of diffraction and direction of travel). After all photons (transmitted and reflected) have exited the lens, an absorption correction is applied corresponding to each photon's path length through the lens and the photons' energy.

4.4 Optimized lens design

This section describes the parameters and performance of the optimized Laue-lens system. It makes choices on system parameters described in Section 4.3.

4.4.1 Decisions on the system parameters

Before a design can be optimized, some parameters and limits of the system need to be fixed. These are the total system length, the focal point depth, the minimum radius, the minimal X-ray energy and the source size. A total system length of 4 m has been chosen. This length of the system is larger than most existing systems but should be practical at least for prototype designs, and allows the use of the relatively efficient 400 diffraction order. To get a small enough focal point, a focal point depth of 5 mm has been chosen. A minimum sagittal radius of 50 mm is considered, which is considered as real-

istically achievable. A minimal X-ray energy of 100 keV is chosen, as going lower would result in rapidly increasing photo-electric absorption in silicon. The data shown in Section 4.3.4 shows that 100 keV X-rays could result in a better focus/skin dose ratio than 300 keV, as the lower energy X-rays come in at larger angles. Furthermore, the decision has been made to look for a middle ground between reflected intensity and convergence angle. Finally, the optimization process was performed for a source size of 2 mm, which is deemed realistic for high-intensity X-ray tubes.

4.4.2 Optimization process

The highest achievable reflected intensity for different diffraction orders as a function of d is shown in Figure 4.6. For each value of d, the intensity is shown for the optimal combination of plate length and meridional curvature. A small increase in the total reflected intensity is seen when moving the lens away from the symmetric point (d = 2000 mm) and closer to the focal point. There, the increase in meridional curvature compensates the lower X-ray flux hitting the lens with higher reflected intensity due to an increase in the bandpass of the plates. It is clear that the most critical factor in determining the total reflected intensity is the used diffraction order. It is chosen to only use the first four diffraction orders satisfying our criteria presented in Figure 4.4 (400, 422, 440 and 444). The next diffraction order, 800, would increase the total diffracted flux only by a few percent given that its effective reflectivity is an order of magnitude lower than that of 400. It is thereby decided that it is not worth pursuing this option.

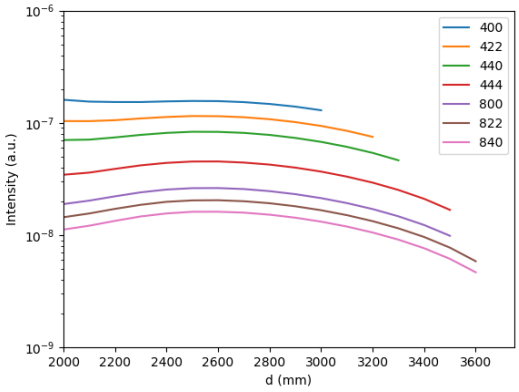


Figure 4.6: Reflected intensity curves of different diffraction orders for a total system length of 4 m and a minimal reflected energy of 100 keV.

Lastly, a decision needs to be made on the position of the lens and the thickness of the SiLC. Planarity and surface roughness usually degrade as silicon wafers thickness becomes smaller. Besides, we want to minimize the number of plates per SiLC.Therefore we chose the maximum thickness allowing the bending and bonding of plates. The plate thickness is fixed to 170 microns based on previous studies[40], and the number of plates determines the thickness of the SiLC. It has been shown in Section 4.3.4 that the conver-

gence angle is of great importance for the focus/skin dose ratio. The convergence angle can be maximized by placing the lens as close to the focus as possible. Figure 4.6 shows that using the 400 diffraction order, the closest the lens can be placed to the source is as $d = 3000$ mm.

Figure 4.7 shows for each value of d what range of r would be occupied by a SiLC of the four chosen diffraction orders. It shows intuitively that a significant gain in convergence angle can be attained by placing the lens at $d = 3000$ mm, therefore this position is adopted in the lens design. It must be ensured that the SiLCs do not overlap radially at this position, which results in the choice of 100, 85, 70, and 120 plates for the 400, 422, 440, and 444 diffraction order, respectively. These choices result in the lens design of which all parameters are listed in Table 4.2.

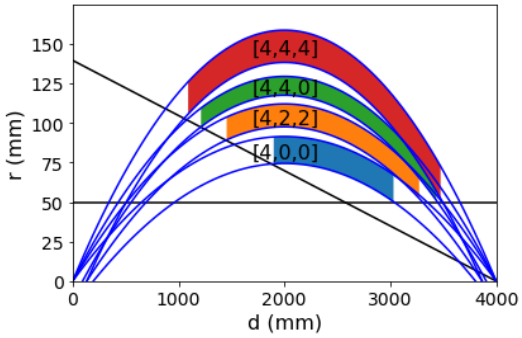


Figure 4.7: Range of r at which the SiLCs of the lens design are located as a function of d. The colored areas denote the allowed positions of each SiLC within the system constraints.

Table 4.2: The parameters of the final lens design used in Monte Carlo method and Geant4 simulations. All rings are made of silicon plates 170-micron thick and 60-mm wide.

	Ring 1	Ring 2	Ring 3	Ring 4
hkl	400	422	440	444
Inner radius (mm)	51.6	69.6	85.3	98.8
Number of plates	100	85	70	120
Plate length (mm)	23.5	25.0	24.5	25.0
Initial angle (°)	0.98	1.33	1.62	1.88
Wedge (arcsec)	11.63	11.59	11.55	11.49
Angular width (arcmin)	2.75	3.76	4.41	5.70

4.4.3 Performance

The performance of the lens system has been assessed using first SSC simulations and then Geant4 for dose calculations. These simulations were performed for a X-ray tube

source operating at 200 kV with a source diameter of 2 mm calculated with SpekCalc software[41–43]. The resulting reflected spectrum is shown in Figure 4.8. It shows that the lens diffracts X-rays between 100 keV and 135 keV. The peak intensity is around 100 keV, as the design imposes that all SiLCs reflect here. Around 115 keV and 122 keV, two large steps in the reflected intensity are observed. These large steps are caused by some SiLCs having a smaller bandpass than others, so at these energies some SiLCs in the lens stop contributing the diffracted spectrum. Also, the peak of the bremsstrahlung in the source spectrum is around 85 keV. The diffracted spectrum of Figure 4.8 lies close to this peak. An X-ray tube operating at a slightly higher voltage could be used as a small optimization.

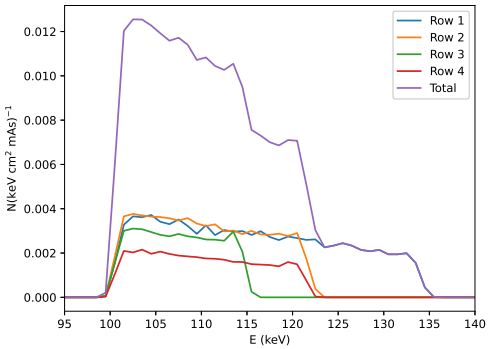


Figure 4.8: The spectrum reflected by the lens design using a 200 kVp X-ray tube source. This spectrum is generated by Monte Carlo method simulations.

To account for attenuation and estimate the dose deposition rate of this system, we performed Geant4 simulations with Monte Carlo data. A phase space file produced by the lens code is imported in Geant4 with positions, directions, energy, and intensity coefficient of each photon diffracted by the lens. SSC simulations have been performed using an X-ray source with a diameter of 2 mm. The X-ray profile 10 cm before the focal point is shown in Figure 4.9. The X-rays coming from each SiLC can still be separated very well.

Figure 4.10 shows the X-ray profile at the focal point. It shows how the X-ray flux intensity is approximately 100 times higher than 10 cm before the focal point.

Figure 4.11 displays a cross-section of the dose deposition in a water phantom, assuming the lens is used with a 3 kW X-ray tube operated at 200 kV (15 mA). The focus is 10 cm deep into the water phantom. It clearly shows a much higher dose rate at the focal point (depth = 100 mm) than at the skin (depth = 0 mm). Note that the dose here refers to the absorbed dose that is the energy deposited per unit mass. The focal spot is cylinder shaped, with a diameter of 0.7 mm and a length of 10 mm.

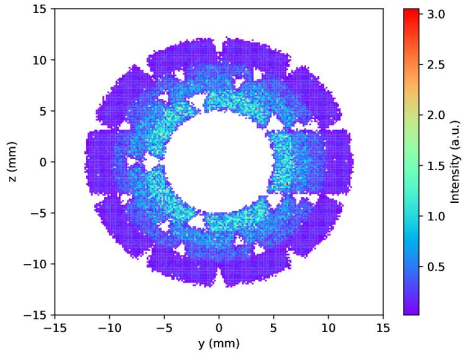


Figure 4.9: X-ray profile 10 cm before the focal point (i.e. at the "skin") for a simulated source diameter of 2 mm.

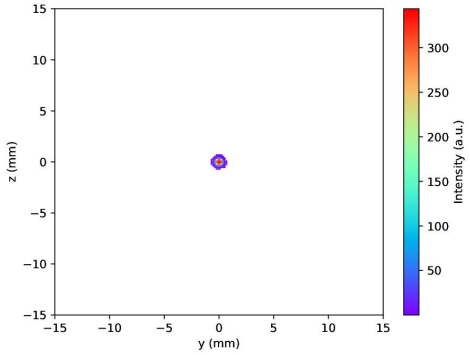


Figure 4.10: X-ray profile at the focal point for a simulated source diameter of 2 mm.

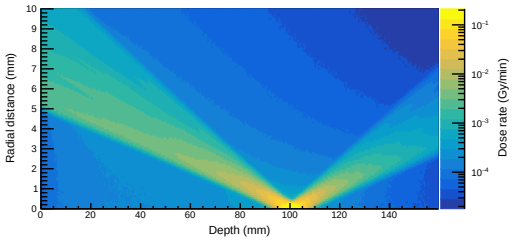


Figure 4.11: Cross section of the dose rate deposition in a water phantom. The optimized lens design was used together with a 2 mm source diameter. This data was generated using Geant4 fed with the output of the python ray-trace code.

Figure 4.12 shows the maximum dose rate delivered as a function of depth into the water phantom. The dose rate at the focal point is 72 times higher than the dose rate at the skin. Using a 3 kW X-ray tube, a dose rate of approximately 0.2 Gy min^{-1} is achieved at the focus.

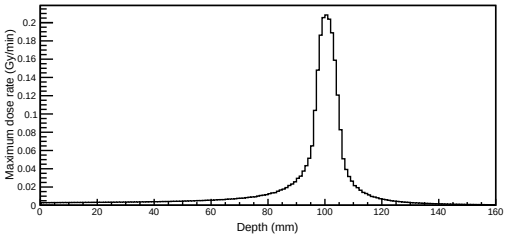


Figure 4.12: Maximum dose rate delivered as a function of depth into a water phantom. The optimized lens design was used together with a 2 mm source diameter. This data was generated using Geant4 fed with the output of the python ray-trace code.

The dose rate we obtain here is ~ 50 lower than in the study of a Laue lens for radiation therapy published by Paternò et al. [16]. This study is complemented by the paper from Camattari [17], which gives details on the treatment of diffraction in crystals that is used to produce this estimated dose rate. The fact that their study is based on a somewhat different Laue lens can not explain the dose rate difference. We concluded after much efforts that their higher dose rate is likely due to an erroneous treatment of diffraction in crystals when the source is placed at finite distance, which was confirmed by the authors [private communication].

4.5 Conclusions and future work

We designed and studied a Laue lens that can focus radiation in a cylindrical volume of 0.7 mm diameter and 10 mm length when coupled to an X-ray tube with a source size of 2 mm diameter. A dose rate of 0.2 Gy/min can be achieved at the focus placed 10 cm within a water phantom considering a 15 mA anode current set to 200 kV. This dose rate is 72 times more than the dose rate at the entrance of the volume. Thus this system can produce a very high focus-to-skin ratio with a small, sharp focus and relatively low dose rate. It should be noted that we studied here an ideal case and that errors in positioning and alignment will affect the performance of an actual system. A sensitivity study will be performed at a later stage.

Several hurdles need to be overcome before this could be translated into a meaningful clinical device. The first is the dose rate. Since a typical radiation therapy treatment requires a dose of approximately 2 to 10 Gy to the tumor in a single fraction, at the dose rates simulated here the treatment time is 10 to 50 minutes. While this is not unreasonable the irradiated volume is a small 0.7×10 mm cylinder whereas typical target volumes might require a $10 \times 10 \times 10$ cm^3 volume. At the current dose rate the time would be pro-

hibitively long if the spot were scanned over this volume, and the skin sparing effect would be reduced. However, the technology is attractive since such a device could be a cost-effective option for treatment tumors particularly where sharp gradients in dose distribution is needed. Given the dose rate and geometry constraints this might be better suited to smaller target regions < 10 cm deep in tissue.

References

[1] D. Girou, E. Ford, C. Wade, *et al.*, *Design and modeling of a laue lens for radiation therapy with hard x-ray photons,* Physics in Medicine & Biology **66**, 245007 (2021).

[2] R. Atun, D. A. Jaffray, M. B. Barton, *et al.*, *Expanding global access to radiotherapy,* (2015).

[3] O. Desouky, N. Ding, and G. Zhou, *Targeted and non-targeted effects of ionizing radiation,* Journal of Radiation Research and Applied Sciences **8**, 247 (2015).

[4] S. Demaria, N. Bhardwaj, W. H. McBride, and S. C. Formenti, *Combining radiotherapy and immunotherapy: A revived partnership,* International Journal of Radiation Oncology Biology Physics **63**, 655 (2005).

[5] C. Allen, S. Her, and D. A. Jaffray, *Radiotherapy for cancer: Present and future,* Advanced Drug Delivery Reviews **109**, 1 (2017).

[6] F. Khan, *The Physics of Radiation Therapy*, LWW Doody's all reviewed collection (Lippincott Williams & Wilkins, 2003).

[7] D. B. Chithrani, S. Jelveh, F. Jalali, *et al.*, *Gold nanoparticles as radiation sensitizers in cancer therapy,* Radiation Research **173**, 719 (2010).

[8] M. K. Leung, J. C. Chow, B. D. Chithrani, *et al.*, *Irradiation of gold nanoparticles by x-rays: Monte Carlo simulation of dose enhancements and the spatial properties of the secondary electrons production,* Medical Physics **38**, 624 (2011).

[9] R. I. Berbeco, H. Korideck, W. Ngwa, *et al.*, *DNA Damage Enhancement from Gold Nanoparticles for Clinical MV Photon Beams,* (2012).

[10] D. Y. Breitkreutz, M. D. Weil, S. Zavgorodni, and M. Bazalova-Carter, *Monte Carlo simulations of a kilovoltage external beam radiotherapy system on phantoms and breast patients:,* Medical Physics **44**, 6548 (2017).

[11] H. Abbas, D. N. Mahato, J. Satti, and C. A. MacDonald, *Measurements and simulations of focused beam for orthovoltage therapy,* Medical Physics **41**, 041702 (2014).

[12] C. Wade, N. Barrière, J. Tomsick, *et al.*, *Construction, characterization, and environmental testing of a Laue lens prototype using Fe and Al crystals,* Nuclear Instruments and Methods in Physics Research Section A: Accelerators, Spectrometers, Detectors and Associated Equipment **895**, 135 (2018).

[13] S. Agostinelli, J. Allison, K. Amako, *et al.*, *GEANT4 - A simulation toolkit,* Nuclear Instruments and Methods in Physics Research, Section A: Accelerators, Spectrometers, Detectors and Associated Equipment **506**, 250 (2003).

[14] J. Allison, K. Amako, J. Apostolakis, *et al.*, *Geant4 developments and applications,* IEEE Transactions on Nuclear Science **53**, 270 (2006).

[15] J. Allison, K. Amako, J. Apostolakis, *et al.*, *Recent developments in GEANT4,* Nuclear Instruments and Methods in Physics Research, Section A: Accelerators, Spectrometers, Detectors and Associated Equipment **835**, 186 (2016).

[16] G. Paternò, M. Marziani, R. Camattari, *et al.*, *Laue lens to focus an X-ray beam for radiation therapy,* Journal of Applied Crystallography **49**, 468 (2016).

[17] R. Camattari, *Laue lens for radiotherapy applications through a focused hard x-ray beam: a feasibility study on requirements and tolerances,* Physics in Medicine and Biology **62**, 7249 (2017).

[18] N. Lund, *A study of focusing telescopes for soft gamma rays,* Experimental Astronomy **2**, 259 (1992).

[19] N. Lund, *An "eSA-affordable" Laue-lens,* Experimental Astronomy **20**, 211 (2005).

[20] H. Halloin, P. von Ballmoos, J. Evrard, *et al.*, *Design and flight performance of a crystal diffraction telescope,* in *Society of Photo-Optical Instrumentation Engineers (SPIE) Conference Series*, Society of Photo-Optical Instrumentation Engineers (SPIE) Conference Series, Vol. 4851, edited by J. E. Truemper and H. D. Tananbaum (2003) pp. 895–904.

[21] F. Frontera and P. von Ballmoos, *Laue Gamma-Ray Lenses for Space Astrophysics: Status and Prospects,* X-Ray Optics and Instrumentation, 2010. Special Issue on X-Ray Focusing: Techniques and Applications, id.215375 **2010**, 215375 (2010), arXiv:1007.4308 [astro-ph.IM] .

[22] N. M. Barrière, J. A. Tomsick, S. E. Boggs, *et al.*, *Developing a method for soft gamma-ray Laue lens assembly and calibration,* Nuclear Instruments and Methods in Physics Research Section A: Accelerators, Spectrometers, Detectors and Associated Equipment **741**, 47 (2014).

[23] G. Roudil, P. Courtois, J. Rousselle, *et al.*, *Laue lens: the challenge of focusing gamma rays,* , 106 (2017).

[24] C. Guidorzi, F. Frontera, G. Ghirlanda, *et al.*, *A deep study of the high–energy transient sky,* Experimental Astronomy (2021), 10.1007/s10686-021-09725-9.

[25] H. Halloin and P. Bastie, *Laue diffraction lenses for astrophysics: Theoretical concepts,* ExpA **20**, 151 (2005).

[26] C. Ferrari, E. Buffagni, E. Bonnini, and D. Korytar, *High diffraction efficiency in crystals curved by surface damage,* Journal of Applied Crystallography **46**, 1576 (2013).

[27] N. V. Abrosimov, A. Lüdge, H. Riemann, *et al.*, *Growth and properties of Ge1-xSix mosaic single crystals for γ-ray lens application,* in *Journal of Crystal Growth*, Vol. 275 (North-Holland, 2005) pp. e495–e500.

[28] R. Smither, K. A. Saleem, M. Beno, *et al.*, *Diffraction efficiency and diffraction bandwidth of thermal-gradient and composition-gradient crystals,* Review of Scientific Instruments **76**, 1 (2005).

[29] V. Bellucci, R. Camattari, V. Guidi, *et al.*, *Self-standing bent silicon crystals for very high efficiency Laue lens,* Experimental Astronomy **31**, 45 (2011).

[30] N. Barrière, P. von Ballmoos, P. Bastie, *et al.*, *Second generation crystals for Laue lens applications,* in *Space Telescopes and Instrumentation II: Ultraviolet to Gamma Ray*, Vol. 6266, edited by M. J. L. Turner and G. Hasinger (SPIE, 2006) p. 62662D.

[31] S. Keitel, C. Malgrange, T. Niemöller, and J. R. Schneider, *Diffraction of 100 to 200 keV X-rays from an Si1-xGex gradient crystal: Comparison with results from dynamical theory,* Acta Crystallographica Section A: Foundations of Crystallography **55**, 855 (1999).

[32] T. R. Lindquist and W. R. Webber, *A focusing X-ray telescope for use in the study of extraterrestrial X-ray sources in the energy range 20-140 keV,* Canadian Journal of Physics Supplement **46**, 1103 (1968).

[33] M. Ackermann, N. M. Barrière, M. J. Collon, *et al.*, *Bending and bonding Si single crystals for high performance Laue lenses,* in *Optics for EUV, X-Ray, and Gamma-Ray Astronomy VI*, Vol. 8861, edited by S. L. O'Dell and G. Pareschi (SPIE, 2013) p. 88610G.

[34] M. Beijersbergen, S. Kraft, R. Günther, *et al.*, *Silicon pore optics: novel lightweight high-resolution X-ray optics developed for XEUS,* in *UV and Gamma-Ray Space Telescope Systems*, Vol. 5488, edited by G. Hasinger and M. J. L. Turner, International Society for Optics and Photonics (SPIE, 2004) pp. 868 – 874.

[35] M. Bavdaz, E. Wille, M. Ayre, *et al.*, *Optics developments for ATHENA,* in *Optics for EUV, X-Ray, and Gamma-Ray Astronomy IX*, Vol. 11119, edited by S. L. O'Dell and G. Pareschi, International Society for Optics and Photonics (SPIE, 2019) pp. 71 – 82.

[36] M. J. Collon, G. Vacanti, N. M. Barrière, *et al.*, *Status of the silicon pore optics technology,* in *Optics for EUV, X-Ray, and Gamma-Ray Astronomy IX*, Vol. 11119, edited by S. L. O'Dell and G. Pareschi, International Society for Optics and Photonics (SPIE, 2019) pp. 150 – 157.

[37] M. Shimbo, K. Furukawa, K. Fukuda, and K. Tanzawa, *Silicon-to-silicon direct bonding method,* Journal of Applied Physics **60**, 2987 (1986).

[38] W. P. Maszara, G. Goetz, A. Caviglia, and J. B. McKitterick, *Bonding of silicon wafers for silicon-on-insulator,* Journal of Applied Physics **64**, 4943 (1988).

[39] C. Malgrange, *X-ray propagation in distorted crystals: From dynamical to kinematical theory,* Crystal Research and Technology **37**, 654 (2002).

[40] D. Girou, C. Wade, N. Barrière, *et al.*, *Development of a second generation SiLC-based Laue lens,* in *Optics for EUV, X-Ray, and Gamma-Ray Astronomy VIII*, Vol. 10399, edited by S. L. O'Dell and G. Pareschi, International Society for Optics and Photonics (SPIE, 2017) pp. 419 – 423.

[41] G. Poludniowski, G. Landry, F. Deblois, *et al., SpekCalc: A program to calculate photon spectra from tungsten anode x-ray tubes,* Physics in Medicine and Biology **54**, N433 (2009).

[42] G. G. Poludniowski and P. M. Evans, *Calculation of x-ray spectra emerging from an x-ray tube. Part I. Electron penetration characteristics in x-ray targets,* Medical Physics **34**, 2164 (2007).

[43] G. G. Poludniowski, *Calculation of x-ray spectra emerging from an x-ray tube. Part II. X-ray production and filtration in x-ray targets,* Medical Physics **34**, 2175 (2007).

5

CONCLUSIONS AND OUTLOOK

This thesis details silicon pore optics (SPO) through its manufacturing process and applications. As described in **Chapter 2**, SPO uses spin-in technology developed for decades by the semiconductor and automotive industry, which have massively invested in the fabrication and processing of silicon wafers. SPO technology has become very mature thanks to the continuous development efforts to prepare the industrial production of Athena[1], the largest X-ray optics yet to be launched into space. In essence, patterned coated silicon substrates are assembled into high-performance, self standing X-ray optics by direct bonding them on top of each other[2, 3]. Direct silicon bonding is key to controlling the paraboloid and hyperboloid shapes of Wolter-type telescope designs[4]. Moreover, the work reported in **Chapter 3** concludes that the combination of thin film metallic coatings and direct silicon bonding is essential to increase the effective area of SPO-based X-ray telescopes[5].From this work, one can infer that SPO technology will extend the breadth and scope of future astrophysical observations. In effect, high-sensitivity observations in the X-ray band are needed to improve the understanding of high-energy phenomena of all classes of astrophysical objects, from large-scale hot gas structures, to compact objects such as black holes. For example, observing the X-ray emitting plasma of the intra-cluster medium would shed light on how hot baryons accrete and evolve [6]. Also, detecting X-ray emissions from accreting super massive black holes with high redshift (z>6) could reveal the processes responsible for their early growth, as well as their influence on larger scales in the early Universe [7–9].

Put another way, this work shows that SPO is a mature technology enabling large space-borne X-ray telescopes by combining large effective area, good angular resolution, and low-mass. However, several challenges remain. First, mirror plate maximum dimensions are constrained by the wafers that are used as base material. Standard silicon wafers come in diameters ranging 50 to 300 mm, each with their own thickness increasing from 275 μm to 775 μm, respectively. At present, the semiconductor industry is widely making use of 300 mm diameter wafers. Larger wafers with 450 mm diameter and 925 μm thickness are emerging, but are not yet widespread due to the significant investments needed to transition mass-processing facilities and tools from 300 mm to 450 mm. Therefore, at present, SPO mirror plates are limited to length shorter than 300 mm, which bounds optical designs they can be used for. At the other end, although there is no clear minimum, it would become difficult to handle plates shorter than ~ 10 mm with the current equipement. Second, the pore height, which is related to the plate length, can be decreased by using thinner wafers. Thinner wafers are produced in smaller series and present higher roughness and larger thickness variations than the standard 300 mm ones, which has, until recently, made them less attractive to use. However, some of these defects can be eliminated with the use of ion beam figuring (IBF), which now offers a way to reduce thickness variations and reduce roughness. Thus, it is possible to think of SPO with mirror plate pitch smaller than 0.775 mm, increasing shell packing density. At the other end, it would also be possible to bond wafers together and then process them. This method opens the possibility to create stacks of mirror plates with double-pitch of 1.55 mm, and would be useful in case of large incidence angles, where the plate length would become too short otherwise. Moreover, SPO stacks replicate the shape of the mandrel, whether it is flat, cylindrical or conical. It can also feature a meridional

curvature, parabolic, hyperbolic, circular, or any other shape. The minimum radius of sagittal curvature is only linked to the material properties, and in turn to the membrane thickness. Membrane thickness of 100 μm has been tested successfully, while 110 μm has been manufactured routinely for Athena. With these thicknesses, the plates can be bent to about 150 mm diameter while remaining comfortably far from critical stress that would lead to breakage. Also, the width and spacing of the ribs determine the open area ratio of the optics, affecting on-axis effective area and vignetting. These parameters affects the final stiffness of the system, and have impact on the optical performance. The higher the density of ribs, the smaller the open area ratio, the stronger the support of the mirror membrane.

In effect, SPO is not only an enabling technology for large space-borne X-ray telescopes such as Athena, it is also a versatile technology that can be further developed for a wide range of applications. For instance, Kirckpatrick-Baez designs or lobster eyes could also be implemented. The technique of replication of a mandrel in self-standing stacks of mirror plates can be used for any medium to large series manufacturing of mirrors, with potentially any figure. For instance, as presented in **Chapter 4**, SPO technology is being actively developed to create advanced gamma-ray focusing elements via the use of diffraction in the volume of the crystalline plates. Self-standing single or double-curvature stacks of plates can be used as Laue lens elements providing improved focusing capability compared to other methods. Consequently, we have designed and modeled a novel optical system composed of a Laue lens coupled to an X-ray tube that produces a focused beam in an energy range near 100 keV[10]. One application of this system is radiation therapy where it could enable treatment units that are considerably simpler and lower in cost than present technologies relying on linear accelerators. As descibed in [11], radiation therapy plays an essential role in the treatment of cancer, with more than 60% of patients receiving radiation therapy, mainly in the form of high-energy photons (2-20 MeV), in the course of their disease management. Therapy beams at low energies may also be attractive in their ability to achieve increased sensitivity when used in combination with high-Z nanoparticles. Recent high-profile studies have shown that tumor cell survival is significantly reduced by combining X-ray irradiation with gold nanoparticles [12]. However, it is not currently possible to deliver low-energy irradiation in the clinical setting without unacceptable toxicity to the skin and normal tissue. In our study case, we designed and studied a Laue lens that can focus radiation in a cylindrical volume of 0.7 mm diameter and 10 mm length when coupled to an X-ray tube with a source size of 2 mm diameter. The Laue lens is made of Silicon Laue Components (SiLCs), which exploit the SPO technology. A dose rate of 0.2 Gy/min can be achieved at the focus placed 10 cm within a water phantom considering a 15 mA anode current set to 200 kV. This dose rate is 72 times more than the dose rate at the entrance of the volume. Thus this system can produce a very high focus-to-skin ratio with a small, sharp focus and relatively low dose rate. It should be noted that we studied here an ideal case and that errors in positioning and alignment will affect the performance of an actual system. A sensitivity study will be performed at a later stage. Yet, several hurdles, such as the dose rate, need to be overcome before this could be translated into a meaningful clinical device. Since a typical radiation therapy treatment requires a dose

of approximately 2 to 10 Gy to the tumor in a single fraction, at the dose rates simulated here the treatment time is 10 to 50 minutes. While this is not unreasonable the irradiated volume is a small 0.7 × 10 mm cylinder whereas typical target volumes might require a $10 \times 10 \times 10$ cm^3 volume. At the current dose rate the time would be prohibitively long if the spot were scanned over this volume, and the skin sparing effect would be reduced. However, the technology is attractive since such a device could be a cost-effective option for treatment tumors particularly where sharp gradients in dose distribution is needed. Given the dose rate and geometry constraints this might be better suited to smaller target regions < 10 cm deep in tissue. Also, with the increasing use of MRI machines, it is predicted that tumors will be detected at earlier stages in the future, which would make such a tool well suited to treat them.

Finally, the work presented in **Chapter 4** can be extrapolated to X- and gamma-ray astronomy[13, 14], a field that could also benefit from SiLC. For example, hard X-ray astronomy in the energy range up to 200 keV is currently limited by the low signal to noise ratio above ~78 keV, at which point the effective area afforded by the current generation multilayer mirrors decreases quickly[15], while the background does not. Laue lenses use Bragg diffraction to concentrate gamma-rays and therefore decouple the collecting area and the detector volume leading to an increase in sensitivity. Furthermore, many areas of astrophysics would, benefit significantly from new observational constraints in the 78 - 200 keV range. Polarization measurements combined with timing capabilities could distinguish between competing models for pulsar magnetospheres; the emission mechanisms in the jets of microquasars and AGN could be distinguished (synchrotron or inverse Compton); Also, the regions of strong gravitational fields near black holes where high-energy emission is produced could be studied.

Ultimately, the silicon pore optics technology is a maturing solution for high-energy optical systems. With further advances, this technology can enable more applications that require imaging and focusing of high-energy radiation.

References

[1] K. Nandra, D. Barret, X. Barcons, *et al., The Hot and Energetic Universe: A White Paper presenting the science theme motivating the Athena+ mission,* arXiv e-prints , arXiv:1306.2307 (2013), arXiv:1306.2307 [astro-ph.HE] .

[2] M. Shimbo, K. Furukawa, K. Fukuda, and K. Tanzawa, *Silicon-to-silicon direct bonding method,* Journal of Applied Physics **60**, 2987 (1986).

[3] W. P. Maszara, G. Goetz, A. Caviglia, and J. B. McKitterick, *Bonding of silicon wafers for silicon-on-insulator,* Journal of Applied Physics **64**, 4943 (1988).

[4] H. Wolter, *Spiegelsysteme streifenden Einfalls als abbildende Optiken für Röntgenstrahlen,* Annalen der Physik **445**, 94 (1952).

[5] D. Girou, S. Massahi, D. D. M. Ferreira, *et al., Plasma etching for the compatibility of thin film metallic coatings and direct bonding of silicon pore optics,* Journal of Applied Physics **128**, 095302 (2020), https://doi.org/10.1063/5.0010212 .

[6] A. V. Kravtsov and S. Borgani, *Formation of Galaxy Clusters,* araa **50**, 353 (2012), arXiv:1205.5556 [astro-ph.CO] .

[7] Y. Li, L. Hernquist, B. Robertson, *et al., Formation of z∼6 Quasars from Hierarchical Galaxy Mergers,* apj **665**, 187 (2007), arXiv:astro-ph/0608190 [astro-ph] .

[8] M. C. Begelman, M. Volonteri, and M. J. Rees, *Formation of supermassive black holes by direct collapse in pre-galactic haloes,* mnras **370**, 289 (2006), arXiv:astro-ph/0602363 [astro-ph] .

[9] M. Volonteri and M. C. Begelman, *Quasi-stars and the cosmic evolution of massive black holes,* Monthly Notices of the Royal Astronomical Society **409**, 1022 (2010), http://oup.prod.sis.lan/mnras/article-pdf/409/3/1022/3833646/mnras0409-1022.pdf .

[10] D. Girou, E. Ford, C. Wade, *et al., Design and modeling of a laue lens for radiation therapy with hard x-ray photons,* Physics in Medicine & Biology **66**, 245007 (2021).

[11] R. Atun, D. A. Jaffray, M. B. Barton, *et al., Expanding global access to radiotherapy,* (2015).

[12] D. B. Chithrani, S. Jelveh, F. Jalali, *et al., Gold nanoparticles as radiation sensitizers in cancer therapy,* Radiation Research **173**, 719 (2010).

[13] N. Lund, *A study of focusing telescopes for soft gamma rays,* Experimental Astronomy **2**, 259 (1992).

[14] N. Lund, *An "eSA-affordable" Laue-lens,* Experimental Astronomy **20**, 211 (2005).

[15] F. A. Harrison, W. W. Craig, F. E. Christensen, *et al., The Nuclear Spectroscopic Telescope Array (NuSTAR) Mission,* Astrophysical Journal **770**, 103 (2013), arXiv:1301.7307 .

SUMMARY

This thesis examines silicon pore optics (SPO) by studying its manufacturing process, applications, and prospects. SPO uses spin-in technology developed for decades by the semiconductor industry, which have massively invested in the fabrication and processing of silicon wafers. In essence, patterned coated silicon substrates are assembled into high-performance, self standing X-ray optics by direct bonding them on top of each other. Direct silicon bonding is key to controlling the paraboloid and hyperboloid shapes of Wolter-type telescope design. Moreover, the combination of thin film metallic coatings and direct silicon bonding is essential to increase the effective area of SPO-based X-ray telescopes that will survive launch and space flight conditions, and therefore extend the breadth and scope of future astrophysical observations. For instance, high-sensitivity observations in the X-ray band are needed to improve the understanding of high-energy phenomena of all classes of astrophysical objects, from large-scale hot gas structures to compact objects such as black holes.

SPO technology has become very mature thanks to the continuous development efforts to prepare the industrial production of Athena, the largest X-ray optics yet to be launched into space. In effect, SPO is not only an enabling technology for large space-borne X-ray telescopes such as Athena, it is also a versatile technology that can be further developed for a wide range of applications. The technique of replication of a mandrel in self-standing stacks of mirror plates can be used for any medium to large series manufacturing of mirrors with potentially any figure. SPO-based Laue lenses, also known as silicon Laue components (SiLC), are being actively developed to create advanced gamma-ray focusing elements via the use of diffraction in the volume of the crystalline plates. Self-standing single or double-curvature stacks of plates can be used as Laue lens elements providing improved focusing capability compared to other methods.

For instance, we have designed and modeled a novel optical system composed of a Laue lens coupled to an X-ray tube that produces a focused beam in an energy range near 100 keV. One application of this system is radiation therapy as it plays an essential role in the treatment of cancer. However, it is not currently possible to deliver low-energy irradiation in the clinical setting without unacceptable toxicity to the skin and normal tissue. SPO-based Laue lenses are a potential solution as they can produce a high focus-to-skin ratio with a small, sharp focus and relatively low dose rate. Yet, several hurdles, such as the dose rate, need to be overcome before this could be translated into a meaningful clinical device.

Ultimately, the silicon pore optics technology is a maturing solution for high-energy optical systems. With further advances, this technology can enable more applications that require imaging and focusing of high-energy radiation.

SAMENVATTING

In dit proefschrift wordt de technologie van de siliciumporiënoptieken (SPO) onderzocht door het fabricageproces, toepassingen en vooruitzichten te bestuderen. De SPO-technologie bouwt voort op technologie die tientallen jaren lang is ontwikkeld door de halfgeleiderindustrie, welke massaal heeft geïnvesteerd in de fabricage en verwerking van siliciumplaten. In essentie worden siliciumsubstraten met een gemaskeerde deklaag geassembleerd tot hoogwaardige, losstaande röntgenoptieken door ze direct op elkaar te hechten. Directe siliciumbinding is de sleutel tot het beheersen van de paraboloïde en hyperboloïde vormen van het Wolter-type telescoopontwerp. De combinatie van dunne-film metallische deklagen en directe siliciumbinding is essentieel om het effectieve verzameloppervlak te vergroten van op SPO gebaseerde röntgentelescopen die lancering naar en de omstandigheden in de ruimte kunnen weerstaan, en daarmee de breedte en reikwijdte van toekomstige astrofysische waarnemingen uit te breiden. Zeer gevoelige waarnemingen in het röntgengebied zijn noodzakelijk om het begrip van hoog-energetische verschijnselen van alle klassen van astrofysische objecten te verbeteren, van grootschalige hete gasstructuren tot compacte objecten zoals zwarte gaten.

De SPO-technologie is volwassen geworden dankzij de voortdurende ontwikkelinspanningen ter voorbereiding op de industriële productie van Athena, de grootste röntgenoptiek voor in de ruimte ooit. In feite is SPO niet alleen de technologie die grote röntgentelescopen in de ruimte zoals Athena mogelijk maakt, het is ook een veelzijdige technologie die verder kan worden ontwikkeld voor een breed scala aan toepassingen. De techniek van het repliceren van een mal tot losstaande stapels spiegelplaten kan worden gebruikt voor middelgrote tot grote serieproductie van spiegels met een grote verscheidenheid aan vormen. Op SPO gebaseerde Laue-lenzen, ook bekend als silicium Laue-componenten (SiLC), worden actief ontwikkeld om geavanceerde focusserende elementen voor gammastraling te maken die gebruik maken van diffractie in het volume van de kristallijne platen. Vrijstaande stapels platen met enkele of dubbele kromming kunnen worden gebruikt als Laue-lenselementen die de straling beter kunnen concentreren dan met andere methoden mogelijk is.

Zo hebben we bijvoorbeeld een nieuw optisch systeem ontworpen en gemodelleerd dat bestaat uit een Laue-lens gekoppeld aan een röntgenbuis, dat een convergerende straal produceert in een energiebereik rond 100 keV. Een toepassing van dit systeem is bestralingstherapie die een essentiële rol speelt bij de behandeling van kanker. Het is momenteel niet mogelijk om laag-energetische straling toe te dienen in een klinische setting zonder onaanvaardbare toxiciteit voor de huid en omliggende gezond weefsel. Op SPO gebaseerde Laue-lenzen kunnen mogelijk een oplossing leveren, omdat ze een hoge verhouding van bestralingssterkte in het brandpunt en op de huid kunnen leveren met een klein, scherp brandpunt en een relatief lage bestralingssterkte daarbuiten. Er

moeten echter nog verschillende hordes genomen worden, zoals het verder verlagen van de bestralingssterkte, voor dit omgezet kan worden in een zinvol klinisch apparaat.

De technologie van de siliciumporiënoptiek is een doorontwikkelende oplossing voor optische systemen voor hoge energie. Met verdere vooruitgang kan deze technologie meer toepassingen mogelijk maken die beeldvorming en concentratie van hoog-energetische straling vereisen.

LIST OF PUBLICATIONS

5. D.A. Girou, E. Ford, C. Wade, C.v. Aarle, A. Uliyanov, L. Hanlon, J.A. Tomsick, A. Zoglauer, M.J. Collon, M.W. Beijersbergen, and N.M. Barrière, *Design and modeling of a Laue lens for radiation therapy with hard x-ray photons*, Physics in Medicine & Biology, 66, 24 (2021).

4. D.A. Girou, C.v. Baren, I.t. Kloeze, L. Castiglione, B. Okma, G. Vacanti, E. Hauser, L. Babić, A. Bayerle, N.M. Barrière, N. Eenkhoorn, R. Günther, Y. Jenkins, B. Landgraf, L. Keek, A. Thete, S. Verhoeckx, M. Vervest, L. Voruz, M.J. Collon, M.W. Beijersbergen, S. Fransen, G. Campoli, I. Ferreira, E. Wille, M. Bavdaz, F. Marioni, and G. Valsecchi, *Environmental testing of the Athena telescope mirror modules*, Proc. SPIE 11822, Optics for EUV, X-Ray, and Gamma-Ray Astronomy X, 1182209 (2021).

3. D.A. Girou, S. Massahi, D.D.M. Ferreira, F.E. Christensen, B. Landgraf, B. Shortt, M.J. Collon, and M.W. Beijersbergen, *Plasma etching for the compatibility of thin film metallic coatings and direct bonding of silicon pore optics*, Journal of Applied Physics, 128, 9 (2020).

2. D.A. Girou, B. Landgraf, A. Bayerle, M.J. Collon, L. Babić, N.M. Barrière, R. Günther, E. Hauser, L. Keek, B. Okma, G. Vacanti, S. Verhoeckx, M. Vervest, L. Voruz, M.W. Beijersbergen, E. Wille, M. Bavdaz, S. Fransen, C.v. Baren, A. Eigenraam, and N. More, *Environmental testing of silicon pore optics for Athena*, Proc. SPIE 11119, Optics for EUV, X-Ray, and Gamma-Ray Astronomy IX, 111190K (2019).

1. D.A. Girou, C. Wade, N.M. Barrière, M.J. Collon, R. Günther, L. Hanlon, J.A. Tomsick, A. Uliyanov, G. Vacanti, A. Zoglauer, *Development of a second generation SiLC-based Laue lens*, Proc. SPIE 10399, Optics for EUV, X-Ray, and Gamma-Ray Astronomy VIII, 103991Y (2017).

CURRICULUM VITÆ

Growing up in France, I enrolled in "classes préparatoires aux grandes écoles" in Tours after high school. There I spent three intense years studying mathematics, physics, and philosophy preparing for the highly competitive exam to enter one of the French "grande écoles", and did so in 2010.

From 2010, I attended the "Institut supérieur de mécanique de Paris" (ISAE-Supméca), an engineering school that specializes in mechanics, aeronautics, as well as industrial management, and logistics. During this time, I had the opportunity to spend six months erecting wind turbines in Canyon at the West Texas A&M University. While in Texas, I used a piece of software developed by the Technical University of Denmark (DTU) and later found out that my French school had an exchange agreement with the Danish university, which sparked my interest.

In 2013, I then enrolled at DTU, but preferred studying instrumentation for astrophysics, instead of pursuing wind energy. During this period, I had the privilege to spend some time at the California Institute of Technology (Caltech) in Pasadena as a guest graduate student where I used NuSTAR data (a NASA X-ray space telescope) to study high-mass X-ray binaries. In addition, I started working beside my studies in the astrophysics department of DTU Space together with Finn Christensen, Desiree Della Monica Ferreira, Anders Jakobsen, and Sonny Massahi. There, I was introduced to Athena and the silicon pore optics (SPO) technology and was even able to hold an SPO plate for the very first time (and unintentionally broke it during one of my first experiments). Following this experience, I completed a thesis on multilayer coatings for high-energy astrophysics telescopes that I presented at the SPIE Optics and Photonics conference in San Diego in the summer of 2015. At the conference, I met Max Collon, Giuseppe Vacanti, and Nicolas Barrière, all from a company called cosine, as well as Marcos Bavdaz and Eric Wille from the European Space Agency (ESA). At that time, I was looking for funding to start a PhD in Denmark, and it seems like a collaboration between cosine, ESA, and DTU was very much possible.

In September 2015, I completed the master's degree at DTU, adding up to the engineering degree from ISAE-Supméca, equivalent to a second master's degree, and was hired as a research assistant in the astrophysics department of DTU Space. After a few months though, I found an agreement with cosine and moved to the Netherlands in March 2016. Thanks to Marco Beijersbergen, managing director at cosine and professor at Leiden University, I was soon able to pursue a PhD in parallel to my work.

Since March 2016, I have been evolving in cosine's international setting with experts in various disciplines, developing SPO technology for Athena and Laue lenses. Further-

more, in 2019, I had the opportunity to take part in the International Space University's (ISU) Southern Space Studies Program (SHSSP) taking place in Australia. This program touching on all space disciplines enabled me to grow a solid international, intercultural and interdisciplinary network. More recently, I followed an executive program at the graduate business school INSEAD to complete my technical and scientific background with bigger-picture strategic insights and leadership skills. In the coming years, I hope to combine and build on all these experiences, and contribute to strengthening the link between science, space, and business.

ACKNOWLEDGEMENTS

First and foremost, I would like to express my gratitude to Prof. Dr Marco Beijersbergen, my supervisor, for giving me the opportunity to do research while working at cosine. I want to thank him for his guidance, and for the freedom I was given in my work. My gratitude extends to my co-supervisor Prof. Dr Michel Orrit for his support, and for providing me with an unbiased view on my progress. Also, I would like to thank the Leiden Institute of Physics (LION) for the opportunity to pursue a doctorate degree.

Developing the silicon pore optics technology in general, and in particular for Athena, is an incredible task that dozens of highly skilled technicians, physicists, and engineers have undertaken at cosine for more than 20 years. I wish therefore to express my special thanks to all the past and present members (unfortunately too numerous to list here) of the high-energy optics team at cosine, among which Max Collon, Dr Giuseppe Vacanti, Dr Nicolas Barrière, and Dr Boris Landgraf.

I wish to show my appreciation to ESA as well, and particularly to Dr Marcos Bavdaz, Dr Ivo Ferreira, and Dr Eric Wille for the support and feedback I received over the years during the many extensive reviews.

Silicon pore optics is a versatile technology that can be further developed for a wide range of applications, but doing so besides the efforts for Athena is no small matter. This feat was only made possible for radiation therapy thanks to the invaluable contribution of the following international members of the Laue lens research group: Dr Eric Ford, Dr Colin Wade, Casper van Aarle, Dr Alex Uliyanov, Dr Lorraine Hanlon, Dr John Tomsick, and Dr Andreas Zoglauer.

In addition, my research would have been impossible without the help of many individuals, including Marlies Bonnet, Karin Liang, and Henriëtte van Leeuwen. Thank you all for your patience and for the continuous aid and support you provided during the entirety of my time in the Netherlands.

Finally, I would like to express my gratitude to my friends and former colleagues at the Technical University of Denmark, with whom I started this entire high-energy optics adventure already more than eight years ago, including Dr Finn Christensen, Dr Desiree Della Monica Ferreira, and Dr Sonny Massahi.